A robust computational framework for simulating the dynamics of large assemblies of highly-flexible fibers immersed in viscous flow

Koshakji, Anwar; Chomette, Grégoire; Turner, Jeffrey; Jablonski, Jonathan; Haynes, Aisha; Carlucci, Donald; Giovanardi, Bianca; Radovitzky, Raúl A.

Important note
To cite this publication, please use the final published version (if applicable).
Please check the document version above.

A robust computational framework for simulating the dynamics of large assemblies of highly-flexible fibers immersed in viscous flow

Anwar Koshakji [a,b], Grégoire Chomette [a,b], Jeffrey Turner [d], Jonathan Jablonski [d], Aisha Haynes [d], Donald Carlucci [d], Bianca Giovanardi [a,b,c], Raúl A. Radovitzky [a,b,*]

[a] *Department of Aeronautics and Astronautics, Massachusetts Institute of Technology, United States of America*
[b] *Institute for Soldier Nanotechnologies, Massachusetts Institute of Technology, United States of America*
[c] *Faculty of Aerospace Engineering, Delft University of Technology, Netherlands*
[d] *US Army DEVCOM Armaments Center, United States of America*

ARTICLE INFO

ABSTRACT

The dynamic response of flexible filaments immersed in viscous fluids is important in cell mechanics, as well as other biological and industrial processes. In this paper, we propose a parallel computational framework to simulate the fluid-structure interactions in large assemblies of highly-flexible filaments immersed in a viscous fluid. We model the deformation of each filament in 3D with a C^1 geometrically-exact large-deformation finite-element beam formulation and we describe the hydrodynamic interactions by a boundary element discretization of the Stokeslet model. We incorporate a contact algorithm that prevents fiber interpenetration and avoids previously reported numerical instabilities in the flow, thus providing the ability to describe the complex evolution of large clouds of fibers over long time spans. In order to support the required long-term integration, we use implicit integration of the solid-fluid-contact coupling. We address the challenges associated with the solution of the large and dense linear system for the hydrodynamic interactions by taking advantage of the massive parallelization offered by Graphic Processing Units (GPUs), which we test up to 1000 fibers and 45000 degrees of freedom.

We validate the framework against the well-established response of the sedimentation of a single fiber under gravity in the low to moderate flexibility range. We then reproduce previous results and provide additional insights in the large to extreme flexibility range. Finally, we apply the framework to the analysis of the sedimentation of large clouds of filaments under gravity, as a function of fiber flexibility. Owing to the long time spans afforded by our computational framework, our simulations reproduce the breakup response observed experimentally in the lower flexibility range and provide new insights into the breakup of the initial clouds in the higher flexibility range.

© 2022 Elsevier Inc. All rights reserved.

---

* Corresponding author at: Department of Aeronautics and Astronautics, Massachusetts Institute of Technology, United States of America.
E-mail address: rapa@mit.edu (R.A. Radovitzky).

1. Introduction

Networks of stiff or flexible filaments distributed through soft materials or immersed in viscous fluids occur in several biological systems, from the microscopic scale of cytoskeleton [1] to the macroscopic scale of connective tissue [2]. Biopolymers such as DNA and actin filaments confer their mechanical properties to living cells [3] and are essential for multiple cell functions [4]. Inspired by these complex biomaterials, synthetic filament networks with tunable properties have been designed and manufactured for applications ranging from nanoprobes to soft biomedical devices and constructs for tissue engineering. Some examples include: hard nanocomposites [5,6], soft composites [7], and dynamically reconfigurable multifunctional materials [8]. Flexible fibers can also be dynamically actuated, for example by oscillating magnetic fields, to realize uniflagellar soft robots [9] and microscopic artificial swimmers [10] for drug on-demand delivery systems in the human body. How the microscopic flexible filaments interact collectively [11] and with the surrounding fluid [12], and how these interactions determine the ensemble macroscopic behavior is therefore of broad and significant interest. However, there is still a limited understanding of the response of these coupled, multi-physics systems, due to the complex fluid-structure and contact interactions involved.

Since the pioneering work of Batchelor [13] and Adachi [14], a significant amount of literature [15–30] has been dedicated to the characterization of the sedimentation of particle clouds with a combination of experimental, analytical, and numerical approaches, see for example [31] for a recent review. Perhaps owing to their reduced physical complexity, progress in fundamental understanding has been significant for the case of clouds of spherical particles [13–16,24], spheroidal particles [17], and rigid fibers [18–23,32,33,25] embedded in incompressible viscous flows. Prior work concerned with the sedimentation of particle clouds can also be found in [34–39]. For example, Adachi et al. [14] conducted experiments on the evolution of an initially spherical cloud of particles falling in a viscous fluid and first observed the formation of a vertical tail of particles, trailing from the back of the cloud, depleting the central region of the cloud and leading to the formation of a torus. Metzger et al. [24] showed that the torus would then expand radially over time and, given enough particles, it would bend and break up into smaller clusters at a critical aspect ratio, each of the clusters forming a torus in a repeating cascade. Moreover, it was also found that the sedimentation rate of such clouds of particles is hindered by particle interactions and, hence, decreases as the particle concentration increases [13,16]. Park et al. [25] studied the case of clouds of rigid fibers and observed that an initially spherical cloud also evolves into a torus, which also eventually breaks up in secondary clouds. However, by contrast to the case of spherical particles, the sedimentation velocity increases with fiber concentration [17]. Furthermore, it was observed in both experiments [18,20] and simulations [19,21,22] that fibers tend to align in the direction of gravity, with occasional flipping, and to clump together to form packets, leading to an increase of the cloud sedimentation velocity. Efforts to develop more capable computational models are starting to enable analyses of fiber clouds of weak [40] and moderate [41] flexibility in three dimensions. The case of extremely flexible fibers has apparently only been tackled in two dimensions [41]. In [41], Schoeller et al. have shown that fiber flexibility delays the cluster's break-up and leads to the cloud's disintegration after sufficiently long time. However, it is clear that important physical insights about the effect of flexibility on the dynamics of clouds of fibers immersed in a fluid remain to be unveiled.

The case of a single fiber sedimenting in a viscous fluid has been studied in much more detail. While it is well-known that a rigid fiber settles in a viscous fluid at constant velocity and orientation [17], the sedimentation of flexible fibers leads to a much richer set of responses. Because hydrodynamic interactions along the fiber are stronger near its middle than near its ends, the middle of the fiber is subject to a lower viscous drag. As a result of this nonuniform drag, a flexible fiber will deform and orient with its axis perpendicular to the direction of gravity regardless of the initial configuration [42] and the fiber shape at steady state will depend on the magnitude of gravity relative to fiber elasticity, see [43–45]. More precisely, it was found that this problem can be characterized by a dimensionless elasto-gravitation number representing the ratio of the gravitational and the elastic bending moments. Furthermore, the computational and analytical models used in these studies show that in the weakly-flexible regime the steady-state filament deformation exhibits a U shape, which becomes more pronounced and eventually transitions into a W shape as the flexibility increases. The W shape is found to be marginally stable and depending on the elasto-gravitation number will evolve into a highly distorted horseshoe shape, or into a nonplanar periodic zigzagging motion [43]. The theoretical predictions of [43–45] have recently been observed experimentally with the exception of the transient W shape, which has never been observed experimentally in published work.

Computational analysis provides valuable insights in all those configurations that remain out of analytical or experimental means. A number of approaches have been proposed to model this problem computationally. The Stokes flow equations are usually assumed due to the low Reynolds numbers (very small radius, high viscosity, and moderate flow velocities) and to the flow incompressibility. An effective approach to solve these equations is the so-called slender body theory [46,32,25,44,47,40,48], in which a line distribution of fundamental solutions is used to describe the perturbation to the flow induced by a filament. The deformation of the filaments has been modeled with mainly two very different approaches. One of them is the so-called *beads model* [43,49–53,45,54,55], which is attractive for its simplicity of implementation and ability to incorporate contact mechanics, but has been criticized for the lack of a sound mathematical foundation [56]. A sound formulation, honoring the structural theories of beam bending, especially in the presence of large deformations, is critical for describing some important mechanisms in the response of very flexible filaments, including the role played by shear deformations and geometric effects on the bending stiffness. The second approach describes the fibers deformation with the well-established Euler-Bernoulli beam theory [46,44,40,48]. A major limitation of this linear theory is that it is derived

under the assumption of small deflections, which also prevents access to the important geometric nonlinear effects on the bending stiffness, namely stiffening under tensile axial load and buckling under compression, especially in the case of highly slender fibers.

A major challenge for all computational models is the very large computational cost that arises in the simulation of large assemblies of flexible filaments [46,47]. In the case of rigid fibers, the computational feasibility limit has been incrementally pushed from $\mathcal{O}(100)$ [32], to $\mathcal{O}(500)$ [22] and $\mathcal{O}(1000)$ [25]. By contrast, in the case of flexible fibers and regardless of the fiber model employed, the number of degrees of freedom per fiber required to describe its deformation increases significantly, thus reducing the maximum number of fibers that can be simulated simultaneously. For example, Tornberg et al. [46] were able to simulate the sedimentation of 25 flexible filaments. A widely-employed technique to artificially augment the number of flexible fibers in the model is to use periodic boundary conditions, see for example [46–48]. However, this modeling choice has a significant influence on the resulting behavior of the fiber assembly [22]. It was recognized in [32] that modeling a large number of flexible filaments requires scalable parallel computational capabilities. A recent paper by Nazockdast et al. [40] proposed a parallel computational framework able to simulate the sedimentation of clouds of $\mathcal{O}(1000)$ weakly deformable fibers, using an Euler-Bernoulli beam formulation coupled with slender body theory and a fast multipole method [57].

In this paper, we propose a parallel computational framework to simulate large assemblies of highly-deformable filaments immersed in a viscous fluid with focus on the complex dynamics resulting from the competition of large elastic filament deformation and hydrodynamic and contact interactions. We model the deformation of each filament in 3D with the geometrically-exact large-deformation, finite-element beam model proposed by Meier et al. [58,59]. This includes a third-order Hermite polynomial interpolation in space of the beam elements, as necessary to satisfy the C^1-continuity requirement. For the purposes of fluid-structure interaction response, the infinitely rigid case can be approximated in our computational framework with significantly high values of the fibers stiffness. However, a more appropriate model for this regime would treat the fibers as rigid bodies. The infinitely rigid case has been extensively studied in [25]. However, it is worth emphasizing that our coupled framework is general enough that the filaments model can be replaced by a rigid model without modifications of the fluid and contact models. Following a standard approach, we describe the hydrodynamic interactions by imposing fundamental solutions to the Stokes flow on the centerline of each filament, which relate the local beam velocity and the fluid forces via a system of integral equations. We then discretize the fluid forces with boundary elements [60,40] describing the beam centerline to obtain a linear system of integral equations for the fluid nodal forces. A common discretization approach is to assume element-wise uniform fluid forces [40,60,41], which are usually integrated numerically [40,41]. Smith [60] proposed to use an analytical integration of the nearly-singular integrals, which is exact in the case of straight segments and uniform fluid forces. Here, we propose to increase the accuracy of the numerical approach with linear interpolation of the fluid forces and we show that the resulting integrals can also be calculated analytically on piece-wise segments.

As it is well-known, a major challenge involved with boundary element methods is that their discretization results in dense linear systems. This challenge has been addressed in the literature by the use of a fast multipole approach [40], which brings efficiency improvements by significantly reducing the matrix bandwidth thus allowing to take advantage of parallel preconditioners, or by the use of Broyden's method with a suitable choice of approximate Jacobian [41]. In our formulation, we address the challenges associated with the solution of a large and dense linear system by taking advantage of the massive parallelization offered by Graphic Processing Units (GPUs). In fact, current implementations of dense linear solvers on GPUs enable the scalable solution of large dense linear systems, while also leveraging the robustness of direct solvers, which are oblivious to ill-conditioning issues.

Another considerable challenge that emerges when trying to increase the number of filaments in the assemblies to $\mathcal{O}(1000)$ is that the simulations become numerically unstable due to the singular character of the Stokes equation as fibers come too close to each other [25,40]. In [25], the instability was artificially removed by neglecting the hydrodynamic interactions of filaments when they diverge, at a cutoff distance of one fiber diameter, thus allowing fibers to unphysically cross each other, while in [40] simulations would be simply allowed to terminate early, as soon as the instability was detected. In this work, we address the numerical issues resulting from the singularity of the Stokes equation by observing that contact occurs before the singularity, because the fibers have finite thickness. Specifically, we adopt the state-of-the-art *point-to-point* contact formulation for beams by Wriggers and Zavarise [61], which will prevent fibers interpenetration before the singularity occurs.

Different schemes can be conceived to solve the coupled fluid-structure-contact problem. An additional challenge is that the solid mechanics problem is very highly nonlinear and exhibits buckling instabilities which are accentuated in the range of extreme fiber flexibility sought in this paper. To mitigate the numerical issues that emerge when trying to find equilibrium configurations of the beam structures, we adopt the well-established approach of extending the equilibrium problem to the dynamic range, where inertia and numerical viscosity stabilize the numerical solution and enable an efficient convergence to the equilibrium configuration without introducing any spurious dynamic effects. This creates an apparent inconsistency with the fluid formulation, which is entirely static. However, there is no practical implication of this choice, as the verification and simulation examples show.

After a thorough investigation we concluded that the most computationally efficient approach is a predictor-corrector scheme, where the structural problem is solved with an implicit time integrator (implicit Newmark), the contact forces

and the fluid forces are computed between the predictor and the corrector steps, by solving the contact problem and the steady-state fluid problem at the end of each dynamic time step, respectively.

We perform thorough verification and validation of our model with the analytical results of [62] and [44] and with the experimental results of [52], respectively, for the fiber sedimentation problem discussed above. The sound large-deformation beam formulation allows us to span the parameters space up to extreme aspect ratios and to observe the transition from the U to the W shape. We then apply our computational framework to study how fiber flexibility affects the behavior of a falling cloud of filaments.

The presentation of the work is structured as follows. In Section 2 we present the formulation of the mathematical model for the coupled system, the numerical discretization, and the strategy to solve the resulting coupled dynamic system of equations. In Section 3 we present verification and validation results. In Section 4, we apply the method to study the transition from the U to the W shapes and the sedimentation of a cloud of fibers. Section 5 is devoted to analyzing the performance of the proposed computational framework. In Section 6 we summarize the paper and draw conclusions.

2. Computational framework

The simulation of filaments in a viscous flow requires a computational framework with the capability to model several physical mechanisms: the deformation of the filaments, the fluid flow around the filaments and its interaction with the structures, and as we propose in this paper, the possibility of rigid contact between fibers. In this section we describe the numerical methods adopted and explain the fluid-structure coupling strategy.

2.1. Beam model

In order to simulate extremely slender beams subject to large deformations, we adopt a recent Kirchhoff-Love exact beam formulation proposed by Meier et al. [58,59]. This model exhibits considerable advantages for the regime of very large aspect ratios and allows to access the important nonlinear effects of extremely flexible fibers. More precisely, we adopt a torsion-free formulation with restrictions to initially straight and stress-free beams without axial/torsional moments as external loads. Additionally, for the sake of computational efficiency and consistently with the geometry of the filaments, we assume that the beams have circular and isotropic cross sections. For completeness we briefly summarize the beam model in the following of this section.

Filaments can be fully parametrized by a space curve $(s,t) \rightarrow \mathbf{r}(s,t) \in \mathbb{R}^3$ where s represents an arc-length parametrization of the beam length in the initial configuration, and t refers to the time variable. Considering a beam of length L and a total simulation time T, we have $s \in [0, L]$ and $t \in [0, T]$. In order to shorten the notation, the symbol $(.)' = \frac{\partial}{\partial s}(.)$ is employed to refer to derivatives with respect to the arc length coordinate and $\dot{(.)} = \frac{\partial}{\partial t}(.)$ is adopted to refer to time derivatives. The weak form corresponding to the Kirchhoff-Love torsion-free theory for circular beams in three dimensions, assuming no applied axial/torsional moments and no external loads at the boundaries, is [58,59]:

$$\int_0^L \left[\delta \mathbf{r}^T \rho_{\text{fiber}} A \ddot{\mathbf{r}} \right] ds + \int_0^L [\delta\boldsymbol{\varepsilon} EA\boldsymbol{\varepsilon} + \delta\boldsymbol{\kappa} EI\boldsymbol{\kappa}] ds \quad = \int_0^L \left[\delta \mathbf{r}^T \tilde{\mathbf{f}}^{ext} \right] ds \qquad \forall \delta\mathbf{r}, \tag{1}$$

where ρ_{fiber} is the density of the filament, E is the Young's Modulus, while A and I are respectively the area and the moment of inertia of the circular cross section. The symbol $\{\cdot\}^T$ indicates the transpose of the underlying vector. The external forces are noted $\tilde{\mathbf{f}}^{\text{ext}}$ and include fluid-structure interactions, contact interactions, and gravity. The axial strain $\boldsymbol{\varepsilon}$ and bending curvature $\boldsymbol{\kappa}$ are derived in previous work [58] and their variations are given by:

$$\delta\boldsymbol{\varepsilon} = \frac{\delta \mathbf{r}'^T \mathbf{r}'}{||\mathbf{r}'||}$$

$$\delta\boldsymbol{\kappa} = \frac{||\mathbf{r}'||^2(\delta \mathbf{r}' \times \mathbf{r}'' + \mathbf{r}' \times \delta \mathbf{r}'') - 2(\delta \mathbf{r}'^T \mathbf{r}')(\mathbf{r}' \times \mathbf{r}'')}{||\mathbf{r}'||^4} \tag{2}$$

As a common approach to enforce the C^1 continuity across beam elements, e.g. [58], a finite element discretization based on third order Hermitian polynomials is adopted. The position and the variations of the centerlines are described by:

$$\mathbf{r}(\xi) = \sum_{b=1}^2 N_d^b(\xi)\mathbf{d}^b + \frac{l}{2}\sum_{b=1}^2 N_t^b(\xi)\mathbf{t}^b$$

$$\delta\mathbf{r}(\xi) = \sum_{b=1}^2 N_d^b(\xi)\delta\mathbf{d}^b + \frac{l}{2}\sum_{b=1}^2 N_t^b(\xi)\delta\mathbf{t}^b \tag{3}$$

where l is the length of the initial straight beam element, $\xi \in [-1; 1]$ is a natural coordinate inside the element, and the index $b = 1, 2$ refers to the local node number in each element, with position vector $\mathbf{d}^b$ and tangent vector $\mathbf{t}^b$. The four Hermitian shape functions $N_d^b(\xi)$ and $N_t^b(\xi)$ are defined as:

$$N_d^1(\xi) = \frac{1}{4}(2+\xi)(1-\xi)^2 \quad N_d^2(\xi) = \frac{1}{4}(2-\xi)(1+\xi)^2$$
$$N_t^1(\xi) = \frac{1}{4}(1+\xi)(1-\xi)^2 \quad N_t^2(\xi) = -\frac{1}{4}(1-\xi)(1+\xi)^2 \tag{4}$$

The finite element discretization applied to Equation (1) results in a set of ODEs of the following form [63]:

$$\mathbf{M}\ddot{\mathbf{u}} + \mathbf{f}^{\text{int}}(\mathbf{u}) = \mathbf{f}^{\text{ext}}(\mathbf{u}), \tag{5}$$

where $\mathbf{u}$ refers to the vector containing the position and tangent at all the nodes and $\mathbf{f}^{\text{int}}$ is the vector of the internal elastic forces. The time integration procedure employed to solve the system is developed at the end of the section.

It bears emphasis that including the inertia term in Equation (5) may seem at odds with the Stokes regime of filament sedimentation considered in this paper. However, the inertia term provides a convenient and robust way to numerically follow the complex unsteady path in the sedimentation of the filaments without introducing spurious inertia effects, as will be seen in the results section. In particular, the inertia term regularizes the solution procedure for the resulting system of non-linear equations at each time step and avoids significant numerical issues that arise in the strongly non-linear range of large filament deformations.

It should also be noted that, because the inertia of the filaments is negligible, the inertia term in Equation (5) has no practical implication on the output of our model, as can also be observed from the results presented in Section 3.

2.2. Fluid model

As commonly done for the types of problems of interest to this work, we assume Stokes flow conditions. This can be justified because of the fluid incompressibility in this regime and of the extremely low filament diameters, which results in very low Reynolds numbers.

Several approaches to model a Stokes flow around a slender body have been proposed in the literature. Immersed boundary methods formulate the fluid governing equations on the entire three-dimensional computational domain around the slender body [64–71]. A computationally cheaper alternative is that of boundary integral methods, which formulate the governing equations for the fluid only on the immersed boundary surfaces, instead of the entire fluid domain. These methods cast the Stokes flow equations in the form of integral equations of nonlocal distributions of point forces, torques, and stresses modeling the hydrodynamic interactions [72]. Exploiting the slenderness assumption allows to specialize the boundary integral method into the well-known slender body theory [73,62,74,75] and to further reduce the boundary integral governing equations to a one-dimensional formulation along the body's centerline. This further simplification comes at the additional cost of dealing with nearly-singular integrals over the body centerline. In particular, singular integrals arise when this theory is used to model filaments of infinitesimal radius. Approaches used in previous work to deal with this difficulty have been the application of singularity subtraction techniques [40], or the introduction of a numerical regularization parameter which removes the singularity. These include the regularized Stokeslet method [76–79], and a regularized formulation of slender body theory with no loss of asymptotic accuracy [46]). It bears emphasis that, even after such regularization, the integrals in the formulations are still nearly-singular and require either the use of specialized quadrature formulae [46] or semi-analytical techniques [60].

We model the fluid flow around the flexible fibers with slender body theory for Stokes flow in its original formulation as proposed by Batchelor [62]. Specifically, in our approach we model explicitly the finite (yet small) radius of the filaments.

We consider a suspension of N identical fibers of length L and cross-section radius a immersed in a Stokes flow in a domain $\Omega \in \mathbb{R}^3$. The basic idea of the slender-body theory for Stokes flow is that the disturbance motion of the flow due to the presence of the slender body can be approximated by a suitably chosen line distribution of fundamental solutions, called Stokeslets. A Stokeslet is the Green function for the Stokes flow and represents the velocity of the flow at point $\mathbf{x} \in \Omega$ in direction i resulting from a unit point force applied at $\mathbf{y} \in \Omega$ in direction j, which can be expressed as follows:

$$S_{ij}(\mathbf{x}, \mathbf{y}) = \frac{1}{8\pi\mu}\left(\frac{\delta_{ij}}{D} + \frac{D_i D_j}{D^3}\right). \tag{6}$$

In Equation (6), μ is the fluid dynamic viscosity, δ_{ij} is the Kronecker delta, and $D = |\mathbf{D}|$, where $\mathbf{D} = \mathbf{x} - \mathbf{y}$, is the distance between the two points.

The fluid velocity field is then obtained by superimposing the fundamental solutions for all points of the fiber centerline for all fibers, which results in an integral equation of the form:

$$\mathbf{v}(\mathbf{x}) = \sum_{n=1}^{N} \int_{\mathcal{C}^n} \mathbf{S}(\mathbf{x}, \mathbf{y}) \mathbf{f}^{\text{fluid}}(\mathbf{y}) \, d\mathbf{y}, \qquad \mathbf{x} \in \Omega, \tag{7}$$
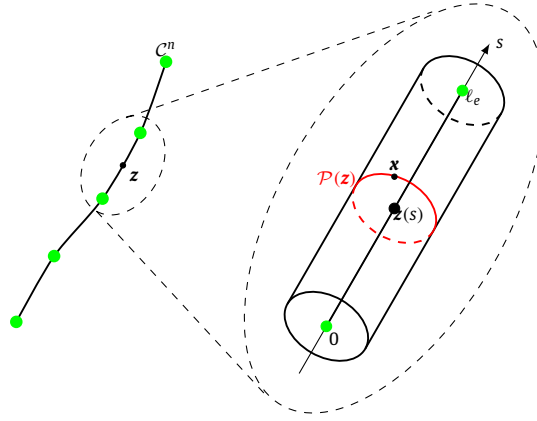
Fig. 1. Schematic of the filament geometry and boundary element discretization.

where $\mathcal{C}^n$ is the centerline of fiber n and $\boldsymbol{f}^{\text{fluid}}(\boldsymbol{y})$ is an appropriate distribution of forces per unit length along the fiber.

It is important to point out that, given a velocity field $\boldsymbol{v}(\boldsymbol{x})$, it is impossible in general to find a distribution of Stokeslets strengths $\boldsymbol{f}^{\text{fluid}}(\boldsymbol{y})$ such that Equation (7) holds for all points on the boundary of the slender body, as higher order singularities are also needed [62]. However, it is well known that Equation (7) approximates the velocity field to the order of ϵ, where $\epsilon = a/L$ is the slenderness parameter, so that higher-order singularities can be neglected when the body is slender [62]. In our case of interest, the typical aspect ratio is at the largest $\epsilon = 1/100$ and possibly smaller, up to $\mathcal{O}(10^{-6})$. In addition, Park et al. [25] have shown that, in order to correctly capture the cloud dynamics, the first-order term of the far-field hydrodynamic interactions is sufficient and that including the short-range interactions is not necessary when the nondimensional parameter $c = \frac{2R}{L}\log\left(\frac{L}{a}\right)$ is small compared to the number of fibers N, where R is the initial radius of the suspension of fibers. Because in our clouds simulations the value of c/N is small ($c/N \approx 0.1$) (see Section 4), the results we present are in a regime in which the higher order terms will not significantly affect the collective dynamics of the suspension.

Equation (7) is coupled with Equation (1) through a relation expressing that the velocity of the fiber be equal to the velocity of the fluid at the fiber boundary (no-slip condition). More precisely, defining $\mathcal{P}(\boldsymbol{z})$ the perimeter of the fiber cross section at a point $\boldsymbol{z} \in \mathcal{C}^n$ on the centerline of fiber n, see Fig. 1, this coupling condition can be expressed as follows:

$$\boldsymbol{v}(\boldsymbol{x}) = \dot{\mathbf{r}}(\boldsymbol{z}) \qquad \forall \boldsymbol{x} \in \mathcal{P}(\boldsymbol{z}), \quad \forall \boldsymbol{z} \in \mathcal{C}^n, \quad \forall n. \tag{8}$$

Using the coupling condition (8), Equation (7) can be rewritten as:

$$\sum_{n=1}^{N}\int_{\mathcal{C}^n} \boldsymbol{S}(\boldsymbol{x},\boldsymbol{y})\boldsymbol{f}^{\text{fluid}}(\boldsymbol{y})\,d\boldsymbol{y} = \dot{\mathbf{r}}(\boldsymbol{z}) \qquad \forall \boldsymbol{x} \in \mathcal{P}(\boldsymbol{z}), \quad \forall \boldsymbol{z} \in \mathcal{C}^n, \quad \forall n. \tag{9}$$

We approximate the integral in the left-hand side of Equation (9) by a sum of straight line integrals on the segments identified by the nodes of the beam formulation of Section 2.1, as follows:

$$\sum_{n=1}^{N}\int_{\mathcal{C}^n} \boldsymbol{S}(\boldsymbol{x},\boldsymbol{y})\boldsymbol{f}^{\text{fluid}}(\boldsymbol{y})\,d\boldsymbol{y} \approx \sum_{n=1}^{N}\sum_{e}\int_{0}^{\ell_e} \boldsymbol{S}(\boldsymbol{x},\boldsymbol{y}(s))\hat{\boldsymbol{f}}(s)\,|\boldsymbol{y}'(s)|\,ds, \tag{10}$$

where ℓ_e is the length of the e-th element, and $\hat{\boldsymbol{f}}(s) = \boldsymbol{f}^{\text{fluid}}(\boldsymbol{y}(s))$.

We can then discretize the forces on each filament segment with piecewise linear shape functions as follows:

$$\hat{\boldsymbol{f}}(s) = \sum_{b} N_f^b(s)\hat{\boldsymbol{f}}^b \tag{11}$$

where $N_f^b(s)$ is the linear shape function associated with node b and $\hat{\boldsymbol{f}}^b$ is the nodal force at each discretization node of the filament. The unknown coefficients $\hat{\boldsymbol{f}}^b$ can be determined by collocating the no-slip condition, i.e. Equation (9), at a point $\boldsymbol{x}^a \in \mathcal{P}(\boldsymbol{z}^a)$ for all nodes $\boldsymbol{z}^a$ of the beam discretization, resulting in the following system of linear integral equations in the unknown coefficients $\hat{\boldsymbol{f}}^b$:

$$\sum_{n=1}^{N}\sum_{e}\sum_{b}\int_{0}^{\ell_e} \boldsymbol{S}(\boldsymbol{x}^a,\boldsymbol{y}(s))\hat{\boldsymbol{f}}^b N_f^b(s)\,|\boldsymbol{y}'(s)|\,ds = \dot{\mathbf{r}}^a \qquad \forall a, \tag{12}$$
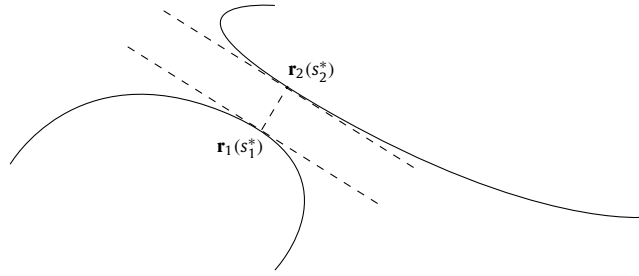
Fig. 2. Minimum distance between the centerlines of two beams.

where we have set $\dot{\mathbf{r}}^a = \dot{\mathbf{r}}(\mathbf{z}^a)$. Expressing Equation (12) in components leads to

$$J_{ai,bj}\hat{f}_j^b = \dot{r}_i^a,\tag{13}$$

where we have set

$$J_{ai,bj} = \sum_{n=1}^{N}\sum_{e}\int_{0}^{\ell_e} S_{i,j}(\mathbf{x}^a, \mathbf{y}(s))N_f^b(s)\,|\mathbf{y}'(s)|\,ds.\tag{14}$$

Note that matrix $\mathbf{J} = \{J_{ai,bj}\}$ is dense and not symmetric. Its components can be computed by evaluating analytically the integrals in Equation (14) for any given point $\mathbf{x}^a \in \mathcal{P}(\mathbf{z}^a)$ for all nodes $\mathbf{z}^a$ of the beam discretization, as described in Appendix A.

2.3. Contact model

As mentioned in the introduction, we use a contact model to prevent fiber interpenetration and avoid the numerical instabilities associated with the singular character of the Stokes equation when the centerlines of two filaments get too close. To this end, we adopt the arguably most popular beam-to-beam contact formulation of Wriggers et al. [61] specifically tailored for large deformations. Additionally, we enhance the contact algorithm with an octree-based spatial search of nearby elements to reduce the time complexity from $\mathcal{O}(N^2)$ to $\mathcal{O}(N\log N)$, where N represents the total number of elements. For completeness, in the following we briefly summarize the formulation of the contact model and the octree-based algorithm.

Considering two flexible filaments of length L and radius a, their centerlines are parametrized at time t and positions s_1 and s_2 by two curves $\mathbf{r}_1(s_1,t)$ and $\mathbf{r}_2(s_2,t) \in \mathbb{R}^3$, and their tangent vectors are noted $\mathbf{r}_{1,s_1}(s_1,t)$ and $\mathbf{r}_{2,s_2}(s_2,t)$. The first step to enforce the contact constraint consists in finding the closest points between the beams at positions s_1^* and s_2^* where contact could potentially occur. Mathematically, this is equivalent to solving the following minimization problem:

$$s_1^*, s_2^* = \operatorname*{argmin}_{s_1,s_2}||\mathbf{r}_1(s_1,t) - \mathbf{r}_2(s_2,t)|| \qquad \forall \quad s_1, s_2 \in [0; L]\tag{15}$$

An approach to tackle this problem was proposed by Wriggers et al. [61], consisting in finding a pair (s_1^*, s_2^*) satisfying the following conditions:

$$\begin{aligned} \mathbf{r}_{1,s_1^*}^T(s_1^*,t)\left[\mathbf{r}_1(s_1^*,t) - \mathbf{r}_2(s_2^*,t)\right] &= 0 \\ \mathbf{r}_{2,s_2^*}^T(s_2^*,t)\left[\mathbf{r}_1(s_1^*,t) - \mathbf{r}_2(s_2^*,t)\right] &= 0 \end{aligned}\tag{16}$$

Essentially, the conditions presented in Equation (16) enforce the orthogonality between the vector joining the two closest points and each of the tangent vectors of the intervening beam segments, as illustrated in Fig. 2. The nonlinear algebraic Equations (16) are solved using Newton's method as in [61]. The incremental problem consists in solving the following linear system:

$$\begin{bmatrix} \mathbf{r}_1'\cdot\mathbf{r}_1' + \Delta\mathbf{r}\cdot\mathbf{r}_1'' & \mathbf{r}_1'\cdot\mathbf{r}_2' \\ -\mathbf{r}_1'\cdot\mathbf{r}_2' & \mathbf{r}_2'\cdot\mathbf{r}_2' + \Delta\mathbf{r}\cdot\mathbf{r}_2'' \end{bmatrix}\begin{bmatrix} \Delta s_1^{i+1} \\ \Delta s_2^{i+1} \end{bmatrix} = -\begin{bmatrix} \Delta\mathbf{r}\cdot\mathbf{r}_1' \\ \Delta\mathbf{r}\cdot\mathbf{r}_2' \end{bmatrix}\tag{17}$$

$$\begin{bmatrix} s_1^{i+1} \\ s_2^{i+1} \end{bmatrix} = \begin{bmatrix} s_1^i + \Delta s_1^{i+1} \\ s_1^i + \Delta s_2^{i+1} \end{bmatrix}\tag{18}$$

where $\Delta\mathbf{r} = \mathbf{r}_2(s_2,t) - \mathbf{r}_1(s_1,t)$. The steps in Equations (17) and (18) are repeated from an original pair (s_1^0, s_2^0) at the center of two elements until convergence is reached. In order to check fiber interpenetration, a parameter p quantifying the minimum distance between the surface of the two elements is defined as:
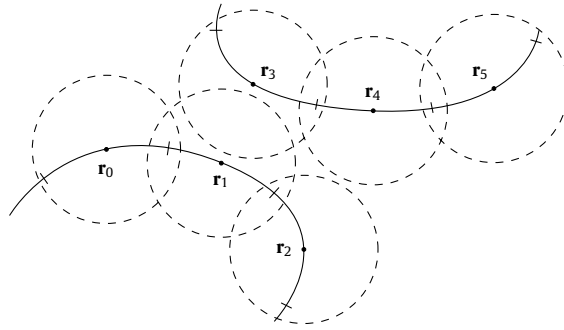
Fig. 3. Illustration of the points $\mathbf{r}_0, ..., \mathbf{r}_5$ representing spatially elements $e_0, ..., e_5$ in the octree data structure. The only non-neighbor elements whose spheres intersect are e_1 and e_3, therefore the minimum distance is searched only for this pair.

$$p := ||\mathbf{r}_1(s_1^*, t) - \mathbf{r}_2(s_2^*, t)|| - 2a$$

If p is negative, the non-penetration constraint is violated and a discrete penalty force is applied to the contact points, proportional to the penetration distance and to the contact's intensity parameter η:

$$\mathbf{f}^{contact}(s_1^*, t) = -\eta p \mathbf{n}_1, \qquad \mathbf{n}_1 = \frac{\mathbf{r}_1(s_1^*, t) - \mathbf{r}_2(s_2^*, t)}{||\mathbf{r}_1(s_1^*, t) - \mathbf{r}_2(s_2^*, t)||} \tag{19}$$

$$\mathbf{f}^{contact}(s_2^*, t) = -\eta p \mathbf{n}_2, \qquad \mathbf{n}_2 = \frac{\mathbf{r}_2(s_2^*, t) - \mathbf{r}_1(s_1^*, t)}{||\mathbf{r}_1(s_1^*, t) - \mathbf{r}_2(s_2^*, t)||} \tag{20}$$

In order to improve the computational efficiency of the contact algorithm, the system presented in Equations (17) and (18) is solved only for a subset of pairs of elements that are found in the vicinity. To this end, we employ an octree-based spatial search method introduced by Meier et al. [63] following the hypothesis that the deformation of an initially straight beam segment of length h remains enclosed in a sphere of diameter h, as illustrated in Fig. 3. The spatial search finds pairs of non-neighbor elements whose spheres intersect, and the nonlinear system of equations to find minimum distances is solved only on this subset. Furthermore, the choice of an octree data structure for spatial search reduces the complexity from $\mathcal{O}(N^2)$ to $\mathcal{O}(N \log N)$, where N represents the total number of elements.

2.4. Time discretization and coupling strategy

Equations (5), (13), and (19)-(20) identify a coupled space semi-discrete system of equations. To summarize, we use third order Hermite polynomial interpolation for the filaments discretization in space, as necessary to satisfy the C^1-continuity requirement across element boundaries, and linear interpolation for the fluid. Finally, we use the traditional second order implicit Newmark scheme to discretize Equation (5) in time. Specifically, advancing the beam deformation $\mathbf{u}$ from time t^n to time t^{n+1} requires solving the following nonlinear coupled problem:

$$\mathbf{M}\ddot{\mathbf{u}}_{n+1} + \mathbf{f}^{int}(\mathbf{u}_{n+1}) = \mathbf{f}^{ext}(\mathbf{u}_{n+1}, \dot{\mathbf{u}}_{n+1}),$$
$$\dot{\mathbf{u}}_{n+1} = \dot{\mathbf{u}}_n + \Delta t((1-\gamma)\ddot{\mathbf{u}}_n + \gamma\ddot{\mathbf{u}}_{n+1}), \tag{21}$$
$$\mathbf{u}_{n+1} = \mathbf{u}_n + \Delta t\,\dot{\mathbf{u}}_n + \frac{1}{2}\Delta t^2((1-2\beta)\ddot{\mathbf{u}}_n + 2\beta\ddot{\mathbf{u}}_{n+1}),$$

where $\beta = 1/4$, $\gamma = 1/2$, $\Delta t = t^{n+1} - t^n$ is the time step, while $\mathbf{u}_n$, $\dot{\mathbf{u}}_n$, $\ddot{\mathbf{u}}_n$, and $\mathbf{u}_{n+1}$, $\dot{\mathbf{u}}_{n+1}$, $\ddot{\mathbf{u}}_{n+1}$ are the approximations of the beam deformation, velocity, and acceleration at times t^n and t^{n+1}, respectively. Note that equation (21) couples the beam deformation with the fluid and contact forces, through the condition:

$$\mathbf{f}^{ext}(\mathbf{u}_{n+1}, \dot{\mathbf{u}}_{n+1}) = \mathbf{f}^{fluid}_{n+1}(\mathbf{u}_{n+1}, \dot{\mathbf{u}}_{n+1}) + \mathbf{f}^{contact}_{n+1}(\mathbf{u}_{n+1}) + \mathbf{f}^{gravity}, \tag{22}$$

where $\mathbf{f}^{gravity} = (\rho_{fiber} - \rho_{fluid})A\mathbf{g}$.

We propose to solve the nonlinear fully-discrete system in Equation (21) with a predictor-corrector scheme, which solves implicitly for the beam deformation, while computing the fluid and contact forces between the predictor and the corrector steps. More precisely, each time step begins with the classic implicit Newmark predictor, which predicts a deformation $\mathbf{u}^0_{n+1}$ and a velocity $\dot{\mathbf{u}}^0_{n+1}$ based on the deformation $\mathbf{u}_n$, velocity $\dot{\mathbf{u}}_n$, and acceleration $\ddot{\mathbf{u}}_n$ obtained at the previous time step. These predictions of deformation and velocities are then used to obtain an approximation of the fluid forces $\mathbf{f}^{fluid}_{n^*}$ and contact forces $\mathbf{f}^{contact}_{n^*}$ at the current time step. The fluid forces at steady state are obtained by solving the dense linear system of Equation (13), while the contact forces are computed through Equations (19)-(20). The iterative corrector step proceeds

then as in the traditional implicit Newmark scheme. Specifically, the deformation, velocity and acceleration are computed incrementally, until convergence, through:

$$\mathbf{u}_{n+1}^{k+1} = \mathbf{u}_{n+1}^k + \Delta\mathbf{u}_{n+1}^{k+1},$$

$$\dot{\mathbf{u}}_{n+1}^{k+1} = \dot{\mathbf{u}}_{n+1}^k + \frac{\gamma}{\beta\Delta t}\Delta\mathbf{u}_{n+1}^{k+1},$$

$$\ddot{\mathbf{u}}_{n+1}^{k+1} = \ddot{\mathbf{u}}_{n+1}^k + \frac{1}{\beta\Delta t^2}\Delta\mathbf{u}_{n+1}^{k+1},$$

where the incremental deformation $\Delta\mathbf{u}_{n+1}^{k+1}$ is obtained by solving the following linearized system of equations:

$$\left(\frac{1}{\beta\Delta t^2}\mathbf{M} + \mathbf{K}_{n+1}^k\right)\Delta\mathbf{u}_{n+1}^{k+1} = \mathbf{f}_{n^*}^{\text{fluid}} + \mathbf{f}_{n^*}^{\text{contact}} + \mathbf{f}^{\text{gravity}} - \mathbf{M}\ddot{\mathbf{u}}_{n+1}^k - \mathbf{K}_{n+1}^k\mathbf{u}_{n+1}^k. \tag{23}$$

The iterative algorithm described above is summarized in Algorithm 1.

Algorithm 1 Coupled fluid-structure-contact algorithm.

Given $\mathbf{u}_n$, $\dot{\mathbf{u}}_n$, and $\ddot{\mathbf{u}}_n$, do:

1. Implicit Newmark predictor:
   a Compute $\mathbf{u}_{n+1}^0 = \mathbf{u}_n + \Delta t\,\dot{\mathbf{u}}_n + \frac{1}{2}\Delta t^2(1-2\beta)\ddot{\mathbf{u}}_n$ (predictor)
   b Compute $\dot{\mathbf{u}}_{n+1}^0 = \dot{\mathbf{u}}_n + \Delta t(1-\gamma)\ddot{\mathbf{u}}_n$ (predictor)
   c Set $\ddot{\mathbf{u}}_{n+1}^0 = \mathbf{0}$
2. Solve for $\mathbf{f}_{n^*}^{\text{fluid}}$ the linear system $\mathbf{J}(\mathbf{u}_{n+1}^k)\mathbf{f}_{n^*}^{\text{fluid}} = \dot{\mathbf{u}}_{n+1}^0$
3. Compute the contact forces $\mathbf{f}_{n^*}^{\text{contact}} = \mathbf{f}^{\text{contact}}(\mathbf{u}_{n+1}^0)$ from Eq. (19)-(20)
4. Implicit Newmark corrector (iterate until convergence):
   a Solve the linear system

   $$\left(\frac{1}{\beta\Delta t^2}\mathbf{M} + \mathbf{K}_{n+1}^k\right)\Delta\mathbf{u}_{n+1}^{k+1} = \mathbf{f}_{n^*}^{\text{fluid}} + \mathbf{f}_{n^*}^{\text{contact}} + \mathbf{f}^{\text{gravity}} - \mathbf{M}\ddot{\mathbf{u}}_{n+1}^k - \mathbf{K}_{n+1}^k\mathbf{u}_{n+1}^k$$

   b Update

   $$\mathbf{u}_{n+1}^{k+1} = \mathbf{u}_{n+1}^k + \Delta\mathbf{u}_{n+1}^{k+1}$$

   $$\dot{\mathbf{u}}_{n+1}^{k+1} = \dot{\mathbf{u}}_{n+1}^k + \frac{\gamma}{\beta\Delta t}\Delta\mathbf{u}_{n+1}^{k+1}$$

   $$\ddot{\mathbf{u}}_{n+1}^{k+1} = \ddot{\mathbf{u}}_{n+1}^k + \frac{1}{\beta\Delta t^2}\Delta\mathbf{u}_{n+1}^{k+1}$$

5. Update

   $$\mathbf{u}_{n+1} = \mathbf{u}_{n+1}^{k+1}$$

   $$\dot{\mathbf{u}}_{n+1} = \dot{\mathbf{u}}_{n+1}^{k+1}$$

   $$\ddot{\mathbf{u}}_{n+1} = \ddot{\mathbf{u}}_{n+1}^{k+1}$$


We have implemented the described computational framework in our research code **ΣMIT** [80]. The solution of the linearized system (23) in each iteration is handed to the PETSc library [81], which provides robust implementations of a wide-range of direct and iterative linear solvers, whereas the solution of the dense linear system (13) is handed to *cuSOLVER* [82], a GPU parallel library for decompositions and linear system solutions for both dense and sparse matrices.

3. Framework validation and verification

A recent paper by Marchetti et al. [52] presents a rigorous experimental and computational study of the sedimentation of a flexible filament in a fluid. In order to validate our computational framework, in this section we present a comparison of our numerical results with their experimental data. The experimental setup consists of a single cylindrical fiber of length L, radius a, and density ρ_{fiber} settling in a quiescent viscous fluid of density ρ_{fluid} from an initially straight horizontal and static position, subject to vertical gravitational acceleration g.

It has been found that the different regimes of physical responses are dictated by a dimensionless number B that quantifies the relative magnitude of the beam bending moment resulting from the gravitational forces and the resisting elastic stiffness [43–45]. In turn the scale of the beam bending moment resulting from the gravitational force is determined by $F_g L$, where $F_g = \pi a^2 L(\rho_{\text{fiber}} - \rho_{\text{fluid}})g$, and the resisting elastic stiffness is determined by EI/L, where $I = \frac{\pi a^4}{4}$ is the moment of inertia of the circular cross section. Hence, the elasto-gravitation number B is expressed as follows:
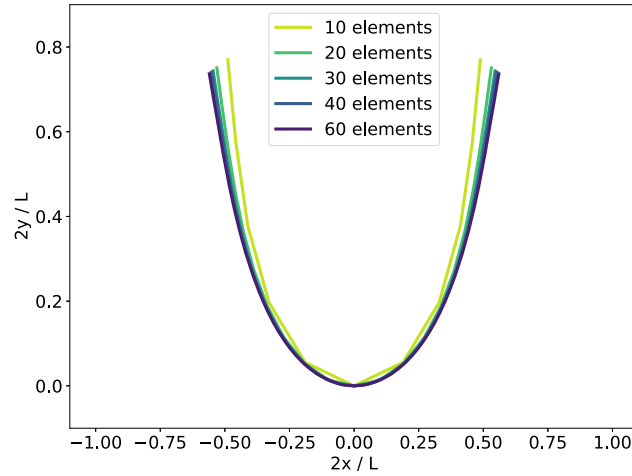
Fig. 4. Mesh convergence analysis for the case $B = 298$. The plot shows the steady-state shapes obtained with different mesh refinements. The magnitude of the displacement difference between the results obtained with 40 and 60 elements per filament is less than 0.5%. (For interpretation of the colors in the figure(s), the reader is referred to the web version of this article.)

Table 1
Parameters of the experiments from [52] used for validation. Each row represents a different experiment in the experimental dataset, which is compared against simulation results obtained for the corresponding value of B.

L [cm]	a [μm]	ρ_{fiber} [kg m^{-3}]	E [kPa]	ρ_{fluid} [kg m^{-3}]	μ [Pa s]	Δt [μs]	B [−]
1.90	232	1617	226	1061	0.30	8	12
2.20	232	1617	226	1061	0.30	15	19
2.50	232	1617	226	1061	0.30	15	28
3.03	232	1617	226	1061	0.30	15	50
3.22	232	1617	226	1061	0.30	25	60
3.83	232	1617	226	1061	0.30	15	101
4.22	232	1617	226	1061	0.30	20	135
5.29	232	1617	226	1061	0.30	20	265
5.19	140	1295	220	1061	0.30	30	298
6.47	232	1617	226	1061	0.30	30	485
7.67	129	1166	218	970	0.97	20	958

$$B = \frac{F_g L^2}{EI} = 4 \frac{L^2}{a^2} \frac{(\rho_{\text{fiber}} - \rho_{\text{fluid}}) \, g \, L}{E} . \qquad (24)$$

We conduct simulations for values of B in the range covered in [52], that is between $B = 60$ and $B = 1000$. Lower values of B result in very stiff, almost rigid filament response. The limit case $B = 0$ corresponds to either the case that $\rho_{fiber} = \rho_{fluid}$, or a combination of parameters for which the beam bending moment resulting from the gravitational forces is negligible compared to the resisting elastic stiffness. The first case corresponds to the neutrally buoyant case. In this case the external forces would be zero and there would be no sedimentation. In the second case, the present formulation would see a decrease of the stable time step in the explicit case, and an increase of the condition number of the jacobians in the implicit case. However, any physically-realistic situation of arbitrary stiffness would be handled without any problems. In the limit of infinite stiffness, which has been considered before, a more appropriate model would treat the fiber as rigid. It is worth emphasizing that our coupled framework is general enough that the filaments model can be replaced by a rigid model without modifications of the fluid and contact models.

The specific parameters of the simulations are summarized in Table 1. In all simulations, we discretize the filament with 20 elements, which we previously verified to provide convergent solutions, see Fig. 4.

Fig. 5 compares the computed steady-state shape of the fibers against the experimental results in [52]. It can be observed that the match between the experimental and the numerical results is overall satisfactory. The discrepancies observed can be explained by potential uncertainty in the parameters used in the simulations, which would require an experimental quantification. In order to illustrate the influence of small variations in the model input parameters, we conducted a series of simulations varying the filament length in the range $[-5\%; +5\%]$ for the case $B = 298$. Fig. 6 presents the steady-state configurations of the filaments obtained. It can be seen that the results are very sensitive to small variations in the filament length.
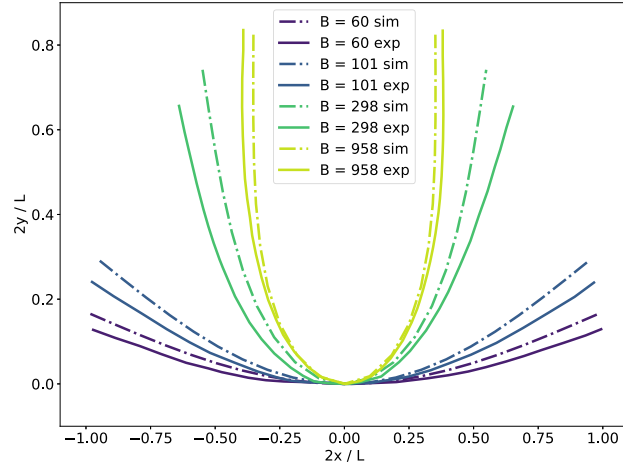
Fig. 5. Experimental vs. simulated steady-state shapes for different values of the elasto-gravitation number B.
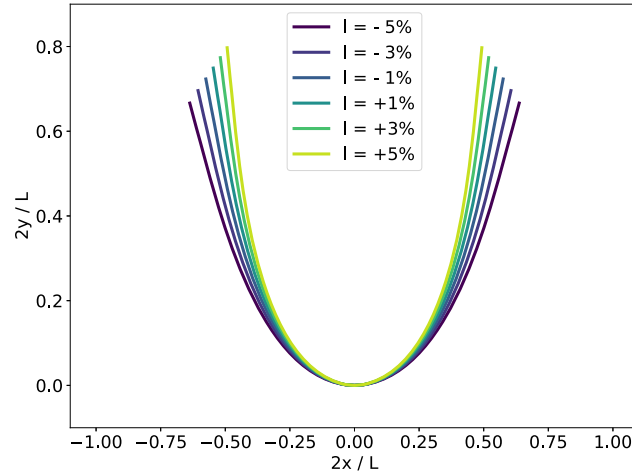
Fig. 6. Sensitivity of the steady-state shape to filament length for $B = 298$.

We also compare the normalized maximum deflection $\frac{2\delta}{L}$ of the steady-state shapes, against experiments and other numerical results [43,52], Fig. 7. It can be seen that the normalized deflection increases with the elasto-gravitation number and then asymptotes to a constant value when a large deformation state is reached ($B \gtrsim 300$).

Finally, we compare the steady-state velocities U obtained in our simulations with experimental data across different flexibility regimes, Fig. 8. In the low-flexibility regime ($B \lesssim 50$) we match the analytical terminal velocity $U_\perp$ of a rigid fiber settling perpendicularly to gravity with less than 1% error, which, according to slender body theory [73] is given by:

$$U_\perp = \frac{\rho g a^2 \left[\log\left(\frac{2L}{a}\right) - \frac{1}{2} \right]}{4\mu}, \tag{25}$$

where $\rho = \rho_{\text{fiber}} - \rho_{\text{fluid}}$. As the fiber flexibility increases, Marchetti et al. [52] observed that the velocities tend to saturate around $\tilde{U} = 1.6 U_\perp$, which we also find in our numerical framework.
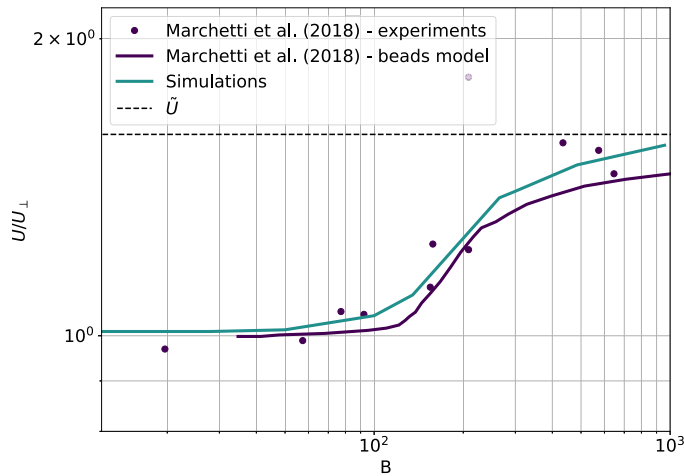
4. Computational experiments

This section presents the results of our computational experiments. Full animations of the time evolution of the simulations in this section are provided in the Supplementary Material.

4.1. Settling of a single highly-flexible fiber

In Section 3, we validated the computational framework against experiments in the weakly-flexible regime ($B \lesssim 1000$). For larger values of B, only computational results are available, due to the difficulty in conducting reliable experiments [52].
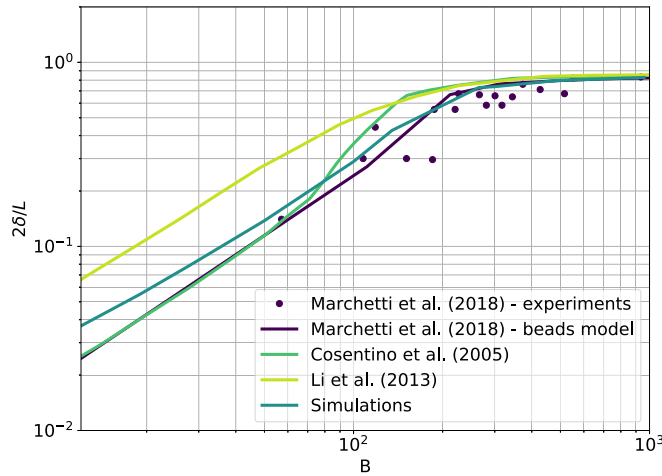
Fig. 7. Experimental vs. simulated normalized maximum deflections for different values of the elasto-gravitation number B. The simulated values are in satisfactory agreement with the experimental results.


Fig. 8. Experimental vs. simulated normalized velocities for different values of the elasto-gravitation number B. The simulated values are in satisfactory agreement with the experimental results.

Prior computational work has shown that in the highly-flexible regime the filament adopts a W shape, before eventually settling into a highly distorted U shape for moderately large B ($B \lesssim 4000$) [43], or a fully 3D, periodic, zig-zagging motion departing from the initial plane for extreme B [43,45]. It is important to mention that the W shape has never been observed experimentally.

Here we repeat those analyses for the purpose of cross verification and extend them to even higher values of B to gain further insights in the nonlinear dynamic response. In the following we show results obtained for $B = 1410$, 4010, 6530 and 8690. For example, a set of physical parameters that realizes such values of B is for filaments of radius $a = 5$ µm, length $L = 0.02$ m, density $\rho_{\text{fiber}} = 2147$ kg/m^3, Young's modulus $E = 19.1$ MPa, 6.7 MPa, 4.1 MPa and 3.1 MPa, respectively, falling under gravity in a fluid with dynamic viscosity $\mu = 10$ µPa s and density $\rho_{\text{fluid}} = 1.0$ kg/m^3. In this case we increase the number of elements to 100 so that more intricate filament deformations can be resolved with sufficient accuracy. Note that we can estimate the Reynolds number for all simulations showed in this paragraph by computing the analytical velocity for a straight beam according to equation (25) [73], leading to $Re = \frac{\rho_{\text{fluid}} U_\perp (2a)}{\mu} \approx 0.1$.

Figs. 9-12 show plots of the vertical velocity of the center of mass $\dot{u}_y^* = \dot{u}_y/U_\perp$ versus time $t^* = t\, U_\perp/L$, along with snapshots of the transient deformed shapes for each simulation at selected times. The snapshots correspond to the states highlighted in the vertical velocity plot by the red dots. We use a time step $\Delta t^* = 0.0005$.

For $B = 1410$, Fig. 9, the filament settles in less than a second into the expected steady state, rather rigid, U shape. It can be seen that the terminal velocity in this case is slightly higher than the theoretical estimate for a straight beam perpendicular to the direction of gravity. For $B = 4010$, Fig. 10, we observe a transitional regime between the U and the W shapes in which the W shape initiates but the fluid forces are not large enough to sustain it against the filament
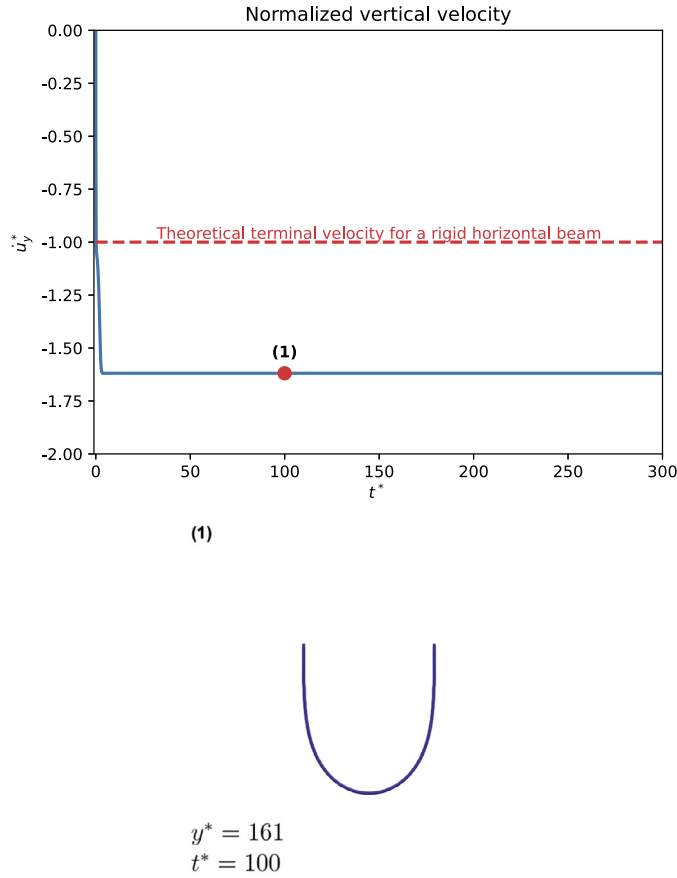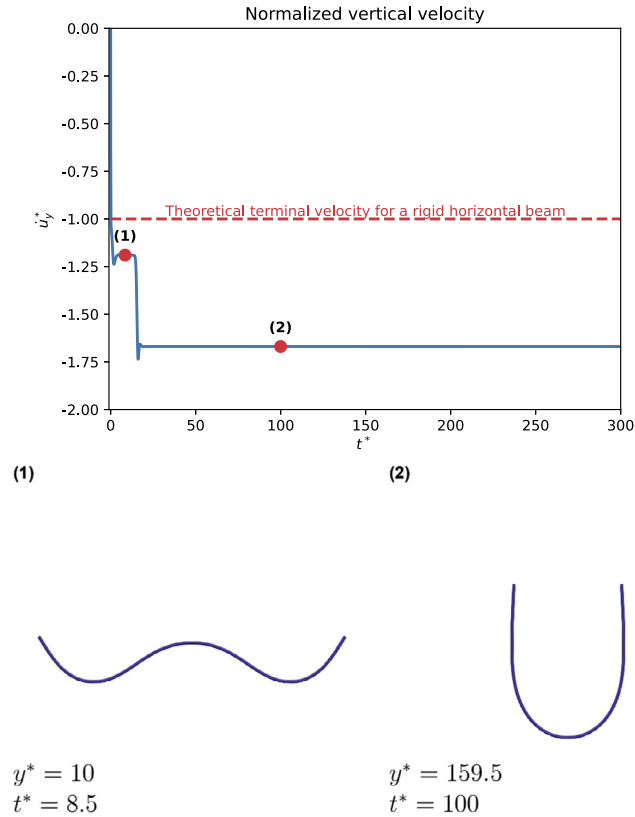
Fig. 9. Simulation of a single filament falling under gravity for $B = 1410$. Top: Plot of the vertical velocity of the center of mass versus time. Bottom: Snapshot of the transient deformed shape. The filament settles into a rather rigid steady-state U shape with a slightly higher terminal velocity than the theoretical estimate for a straight beam perpendicular to the direction of gravity.

elasticity. In fact, this configuration remains stable until $t^* \approx 15$ before falling back into the U shape, which remains steady up to the point where we stopped the simulation at $t^* = 300$. This confirms the results by Lagomarsino et al. [43]. For $B = 6530$, Fig. 11, the response up to $t^* \approx 70$ is qualitatively similar, with a more pronounced W shape that evolves into an apparently stable U shape. However, at $t^* \approx 70$, the filament returns temporarily to an unstable W shape, which lasts for a second and eventually settles into an oscillatory three dimensional motion, in agreement with the predictions of prior computational literature [43,45]. We observe that this periodic motion involves oscillations between a pseudo-U shape and a pseudo-W shapes with secondary components of curvature outside of the initial plane of motion. In this case, there is no terminal velocity but a cyclic value around a mean $\dot{u}_y^* \approx 1.4$. The trend observed in the simulated vertical velocity is that the magnitude increases as the effective length of the filament decreases, yielding lower drag forces acting on the filament. Changes in the filament shape reflect immediately in the velocity as the fluid governing equations are quasi-static and the mass of the filament is very small.

Finally, in the highly-flexible regime ($B = 8690$, Fig. 12) we can clearly identify three phases. Initially, the marginally stable W shape develops, with a more pronounced hump but essentially the same vertical velocity as in the previous cases. After this transient, the filament falls into a periodic motion that alternates U-like and W-like shapes in 2D. In the final phase, the motion becomes distinctly three dimensional and exhibits periodicity, similarly to the previous case. We have conducted simulations for even larger values of B, up to $B \approx 90000$, and observed a qualitatively similar response to that of the last case shown.

We have analyzed the periodic oscillations observed for $B = 6530$ and $B = 8690$ by applying the fast Fourier transform. For $B = 6530$, the fiber eventually settles (Fig. 11 (4)) in a periodic motion with a frequency f of the same order of magnitude of the frequency of the first natural bending mode $f_{n,0}$: $f^* := f/f_{n,0} = 1.38$. For $B = 8690$, the oscillations of the first periodic motion (Fig. 12 (2)) are the superposition of four modes f_i which are very close to the first three natural frequencies of the filament $f_{n,i}$, namely $f_0^* = f_0/f_{n,0} = 1.22$, $f_1^* = f_1/f_{n,1} = 0.85$, $f_2^* = f_2/f_{n,1} = 1.3$, $f_3^* = f_3/f_{n,2} = 0.89$. The frequency of the final periodic motion (Fig. 12 (3)) is $f^* = 1.8$.

Fig. 10. Simulation of a single filament falling under gravity for $B = 4010$. Top: Plot of the vertical velocity of the center of mass versus time. Bottom: Snapshots of the transient deformed shapes. We observe a transitional regime in which the W shape initiates but the filament falls back into the U shape, as the fluid forces are not large enough to sustain the W shape against the filament elasticity.

### 4.2. Numerical instabilities in large clouds of fibers

Recent studies reported numerical instabilities in simulations of large numbers of filaments when the centerlines of two fibers come too close to each other [25,40]. In fact, the fluid model based on Stokeslets (see Equation (6)) presents a singularity leading to unbounded fluid forces as the distance between two fibers or between two portions of the same fiber goes to zero.

In this section, we test the possibility of overcoming these issues via a contact mechanics algorithm that prevents fiber interpenetration. Specifically, we replicate the conditions presented in [40] to simulate a cloud of filaments settling in a viscous fluid, and compare the results with and without contact. The filaments are therefore characterized by an elasto-gravitation number $B \simeq 24$, they are initially straight, randomly oriented and randomly distributed within a sphere of radius $R = 2.5\ L$.

As previously observed in related work [25,40], the simulation without contact forces becomes unstable at the first occurrence of fiber interpenetration. We illustrate this scenario in Fig. 13 where one fiber is violently ejected after coming into contact with another fiber of the cloud. By activating the contact algorithm in the same simulation, the instability disappears and the simulation continues. This improvement in robustness for the computational framework allows to perform simulations involving large assemblies of filaments, which we present in Section 4.3.

4.3. Sedimentation of clouds of flexible fibers under gravity

The problem of characterizing the collective behavior of a sedimenting cloud of particles has been widely studied since the pioneering work by Adachi et al. [14]. In their experiments of spherical swarms of glass particles falling in a glycerol-water solution, Adachi et al. first observed the formation of a vertical tail of particles at the rear of the swarm, the evolution of the assembly into a toroidal shape, and, in certain cases, the suspension break-up into pieces. The breaking up of the suspension was attributed by Adachi et al. and, later by Nitsche and Bachelor [15], to large inertia forces resulting from a large Reynolds number. However, more recently, Metzger et al. [24] revisited those results and demonstrated that an initially spherical cloud is unstable even at low Reynolds numbers for a large enough number of particles. Park et al. [25] analyzed the case of clouds of rigid fibers and showed that an initially spherical cloud of rigid fibers also evolves into a torus, which
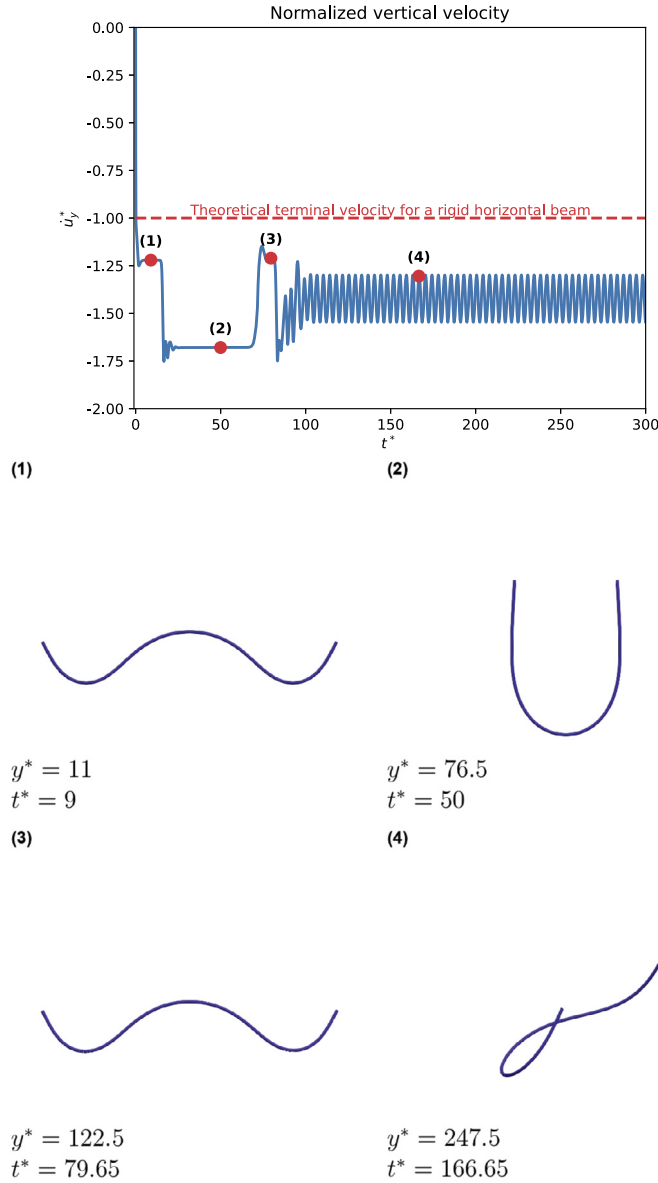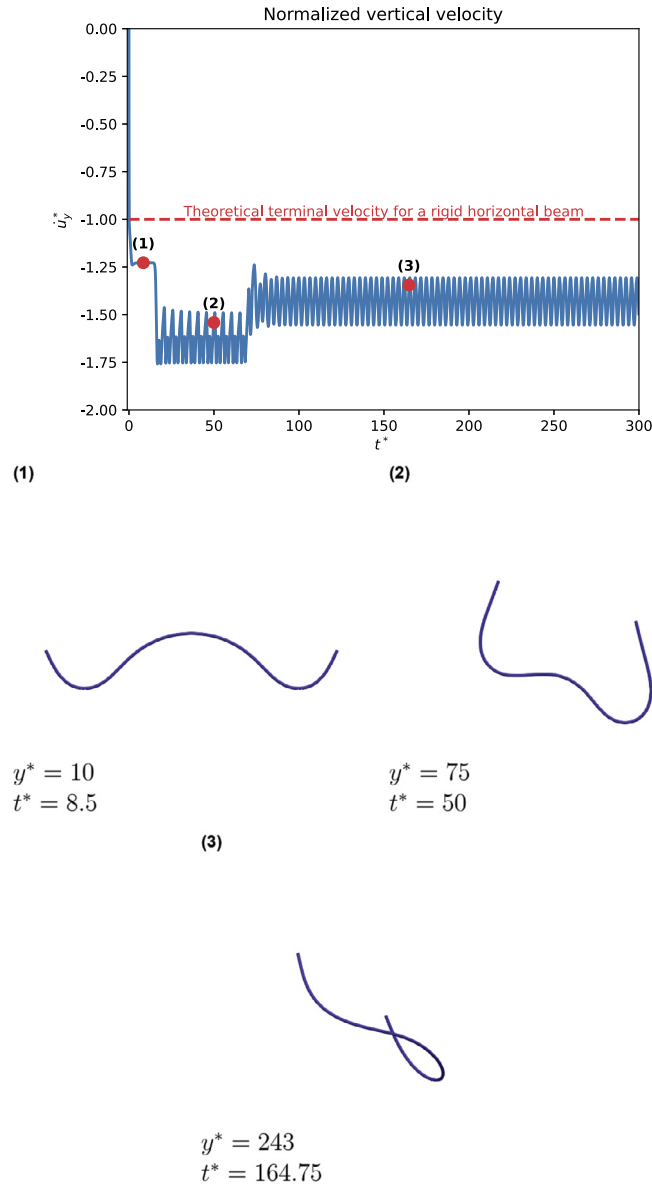
Fig. 11. Simulation of a single filament falling under gravity for $B = 6530$. Top: Plot of the vertical velocity of the center of mass versus time. Bottom: Snapshots of the transient deformed shapes. The W shape initiates and, like in the case for $B = 4010$ (Fig. 10), the filament falls back into the U shape. However, the U shape is only apparently stable. The filament returns temporarily to an unstable W shape and eventually settles into an oscillatory three dimensional motion.

then also breaks into secondary clouds. In recent work, Schoeller et al. [41] have shown that fiber flexibility delays the cluster's break-up and leads to the cloud's disintegration after sufficiently long time.

We apply our computational framework to study how fiber flexibility affects the collective behavior of a cloud of fibers as it sediments in a viscous fluid under gravity. We consider N initially straight fibers randomly distributed in space with their center within a sphere of radius R.

As a starting point, we run a simulation with $N = 128$ and $R = 1.25 L$ in the stiff regime ($B \approx 1$). In Fig. 14, the picture on the left shows the initial cloud in gray and the state of the cloud at $t^* = 4.24$ in blue. We observe a clear trail of filaments, which are vertically aligned and travel slower than the cluster. A zoomed-in view focused on the cluster (right picture) confirms the evolution of the cluster into a toroidal shape in the rigid fiber regime, obtained previously in numerical simulations [25].

We then conduct simulations with different values of $B = 1.177, 11.77, 117.7$ and 1177. We use $N = 200$, and $R = 2.5 L$, with only 6 elements per filament for the two more rigid cases, and 10 and 15 elements per filament, respectively, for the more flexible cases. In all simulations we use a time step $\Delta t^* = 1.41 \ 10^{-5}$.

Fig. 12. Simulation of a single filament falling under gravity for $B = 8690$. Top: Plot of the vertical velocity of the center of mass versus time. Bottom: Snapshots of the transient deformed shapes. The marginally stable W shape develops. After a first transient resulting in the marginally stable W shape, the filament falls into a periodic motion that alternates U-like and W-like shapes in 2D. Eventually, the motion becomes three dimensional, without losing its periodicity.

Fig. 15 shows the trajectories of the clouds for the four simulations. In all cases, we observe from the early stages the formation of the vertical tail at the rear of the cloud, as filaments go across the cloud boundary and are carried downstream. After $t^* = 4.24$, the originally spherical cloud flattens into an oblate shape, which transitions to a toroidal shape and eventually breaks up into smaller clouds. We observe that the higher the flexibility, the less pronounced the toroidal shape. Moreover, as the flexibility increases, additional secondary clouds emerge (3, 4, and 5 distinct secondary clouds for $B = 1$, 10, and 100, respectively). For the highest flexibility ($B = 1000$) the original assembly completely fragments without any noticeable cluster, see also Fig. 16. We also observe that the higher the flexibility, the earlier the assembly break-up occurs, resulting in the slowdown of the assembly. Finally, we observe in Fig. 16 that the clouds with stiffer filaments exhibit secondary tori after the cloud break-up, as observed experimentally by Metzger et al. [24] and Park et al. [25]. It is important to emphasize that the addition of the contact algorithm and the avoidance of the numerical instabilities described in Section 4.2 has enabled the description of the late secondary tori, which was previously inaccessible due to numerical instabilities [40].
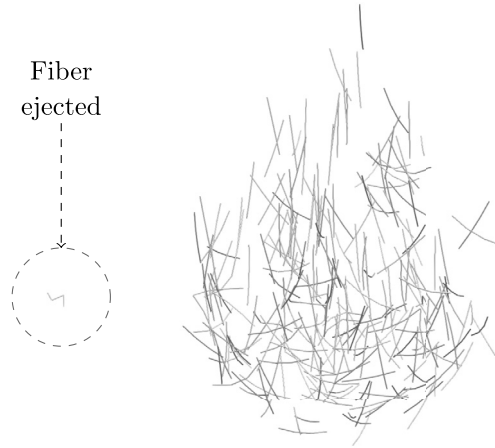
Fig. 13. Example of numerical instabilities resulting from the interpenetration of fibers, sedimenting in a viscous flow under gravity and in the absence of a contact algorithm. Fibers are violently repelled after coming too close to another due to unphysical fluid forces.
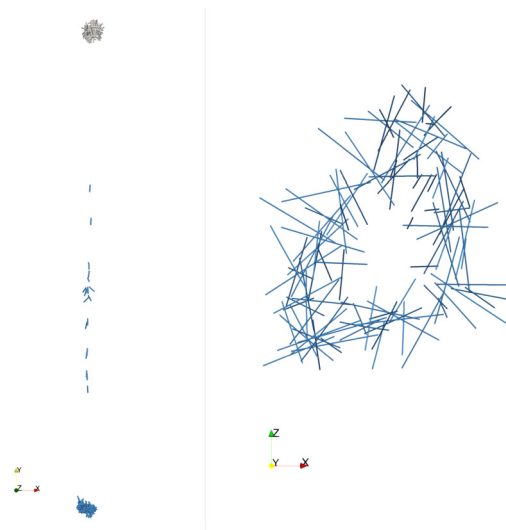
Fig. 14. Simulation results for a cloud of $N = 128$ sedimenting filaments with $B \approx 1$ at $t^* = 4.24$, which corresponds to a traveled distance of 51 R, showing the clear evolution into the well-established toroidal shape. Left picture: Lateral view (initial configuration in gray, deformed configuration in blue). Right picture: Zoom-in of the bottom view, exhibiting the torus formation.

5. Performance of the GPU solver for hydrodynamic interactions

The most computationally intensive part of our algorithm is the solution of the dense linear system for the hydrodynamic interactions (13), for which we employ a GPU implementation of the LU factorization provided by *cuSOLVER* [82]. In order to assess the performance of the *cuSOLVER*, we compare this approach with a serial implementation of the LU factorization solver provided by the *PETSc* library [81] for problems of different size. We run the simulations using an Intel Xeon Gold 6248 CPU with a clock speed of 2.50 GHz and an L3 cache of 28 MB and an NVIDIA TESLA V100 GPU with 5120 CUDA cores, 8.2 TFLOPS for double-precision operations and 32 GB of memory.

In Fig. 17, we plot the computation time of one solution of the fluid linear system for a single filament (simulation setup of Section 3) while varying the number of discretization nodes, thus increasing the total number of degrees of freedom M. We observe that the GPU solver allows to improve performance from $\mathcal{O}(M^3)$ to $\mathcal{O}(M^2)$ and that the GPU solver is more than 300 times faster than the serial one.

6. Conclusions

We presented a parallel computational framework to simulate fluid-structure and contact interactions in large assemblies of highly-flexible filaments immersed in a viscous flow. To model the filaments, we adopted a geometrically-exact large-
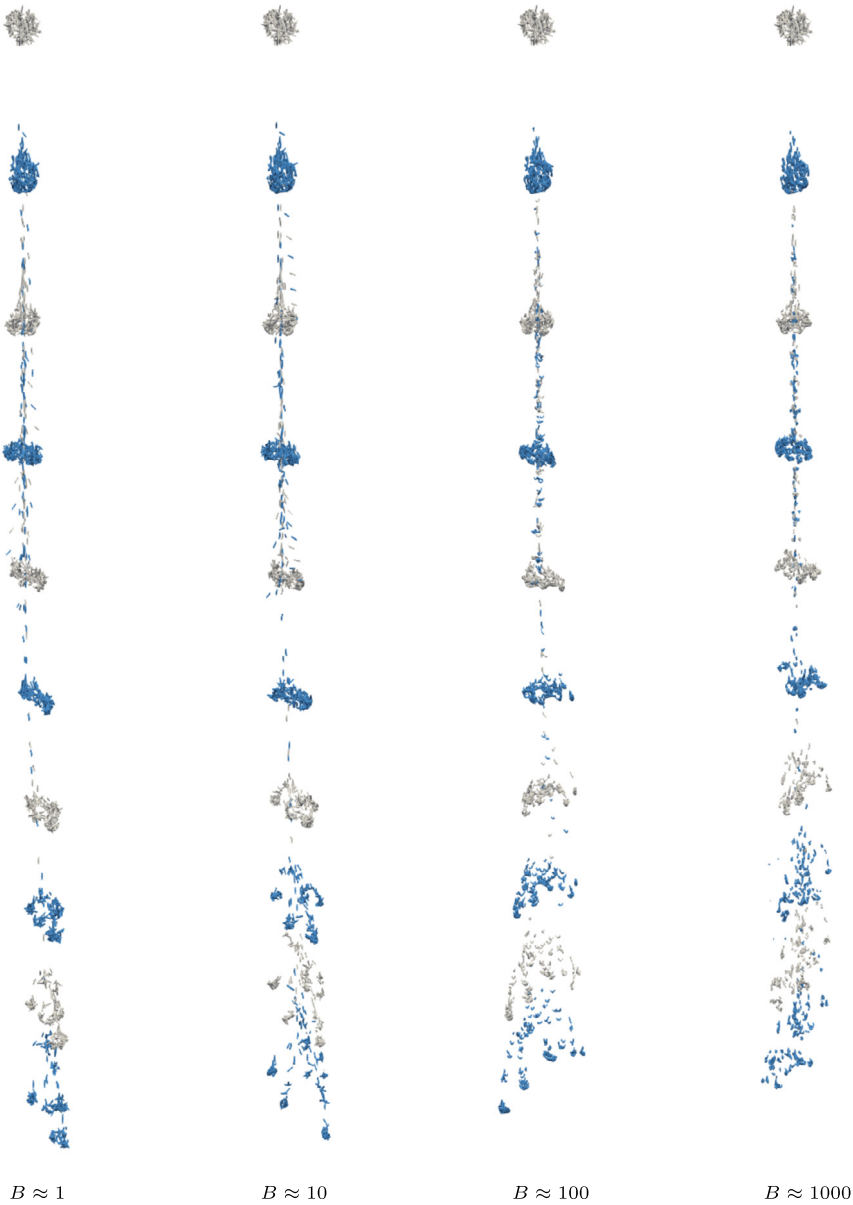
Fig. 15. Evolution of clouds of $N = 200$ filaments for increasing fiber flexibilities, identified by the elasto-gravitation number $B \approx 1$, 10, 100 and 1000. Each row shows the cloud evolution at times increment of $t^* = 1.41$, starting from $t^* = 0$, in alternating solid colors for ease of visualization. The originally spherical cloud flattens into an oblate shape, then transitions to a toroidal shape and eventually breaks up into secondary clusters. The higher the flexibility, the earlier the assembly break-up occurs and the more secondary clusters arise. In the limit of extreme values of B, no defined cluster can be observed, resulting in a more disperse cloud.

deformation beam formulation, which we discretized with C^1 Hermitian finite elements and an implicit Newmark time integrator. We modeled the hydrodynamic interactions with slender body theory for Stokes flow in its original formulation, which we discretized by collocating the equations at the beam discretization nodes and computing the kernel integrals analytically on piece-wise segments approximating the deformed configuration. We overcame previously reported numerical instabilities, arising in the fluid model when fibers came too close to each other, via a state-of-the-art beam contact model suitable for large deformations. We proposed a predictor-corrector scheme to solve the nonlinear fluid-solid coupling, in which the beam deformation is obtained implicitly, while the forces arising from contact and from the fluid-structure interactions are computed after the regular implicit Newmark predictor step. We took advantage of the massive parallelization offered by GPUs to speed up the solution of the large and dense linear system for the hydrodynamic interactions.

We verified and validated our framework against available analytical, numerical, and experimental results for a single filament settling under gravity in the weakly-flexible regime. We explored the dynamical response in the large to extreme flexibility regime. As in previous numerical work, we captured the transition from the characteristic U shape to the W shape

(a) Side view
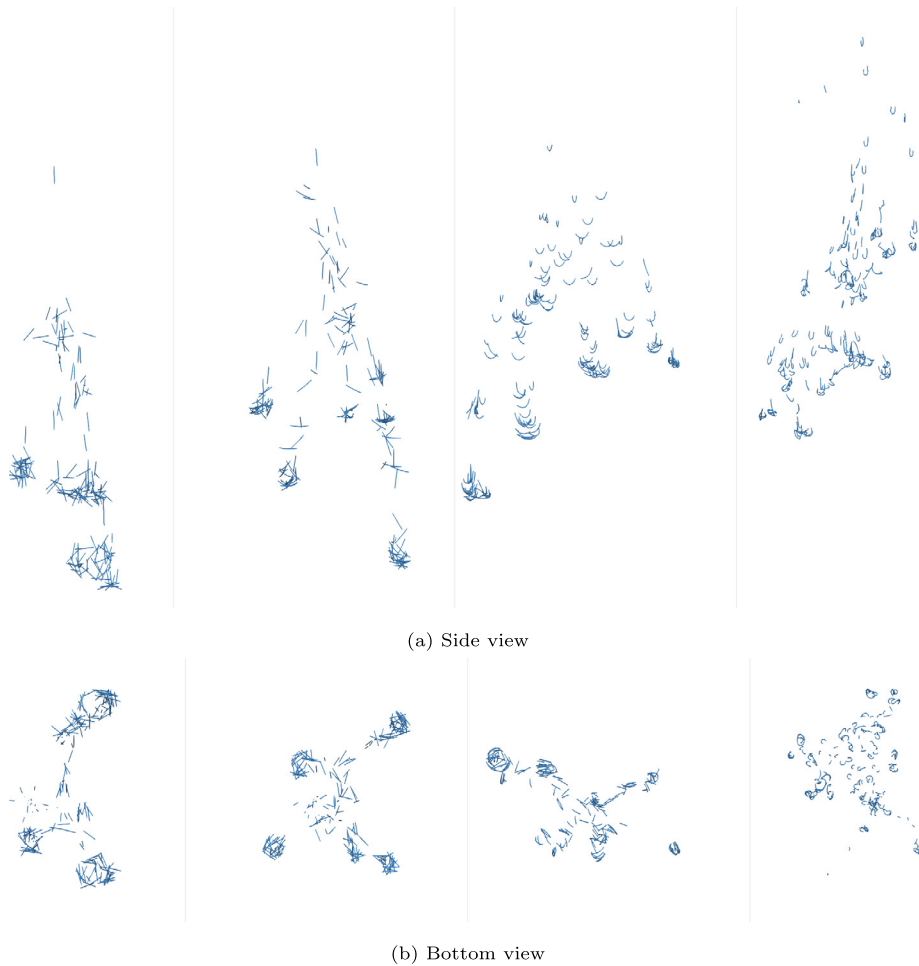
(b) Bottom view

Fig. 16. Detailed (a) side and (b) bottom views of the falling cloud of filaments at the final simulation time $t^* = 12.71$, corresponding to a traveled distance of 60 R, for different flexibilities: $B \approx 1$, 10, 100 and 1000 from left to right. This figure shows that the secondary clusters formed after breakup also adopt toroidal shapes (secondary tori), as observed experimentally by Metzger et al. [24] and Park et al. [25], for the lower flexibility cases (see two left pictures, bottom view).

and found that the W shape is not stable but can either settle back into the U shape, which may in turn transition again to a W shape, or lead to a periodic three-dimensional oscillation, depending on the elasto-gravitation number. We saw that these periodic oscillations prevent the filament from settling into a terminal velocity, but the oscillation frequencies are of the same order of magnitude of the lowest natural frequencies associated with the bending modes of the filament.

Finally, we showed that the contact algorithm enables the simulation of large assemblies sedimenting over long time spans, thus allowing us to extend previous analyses of the complex evolution of clouds of fibers of variable flexibility. A new finding in this problem is that, given enough time, the assembly eventually breaks up into smaller and smaller secondary clusters, as B increases, to the limit, for extremely large B, where no defined cluster can be observed, resulting in a more disperse cloud. The simulations also show that the secondary clusters also adopt toroidal shapes (secondary tori), as previously observed experimentally.

CRediT authorship contribution statement

Anwar Koshakji: Conceptualization, Methodology, Software, Validation, Visualization, Writing – original draft, Writing – review & editing. **Grégoire Chomette:** Methodology, Software, Visualization, Writing – original draft. **Jeffrey Turner:** Validation. **Jonathan Jablonski:** Validation. **Aisha Haynes:** Conceptualization, Validation. **Donald Carlucci:** Conceptualization, Validation. **Bianca Giovanardi:** Conceptualization, Methodology, Software, Supervision, Writing – original draft, Writing – review & editing. **Raúl A. Radovitzky:** Conceptualization, Supervision, Writing – review & editing.
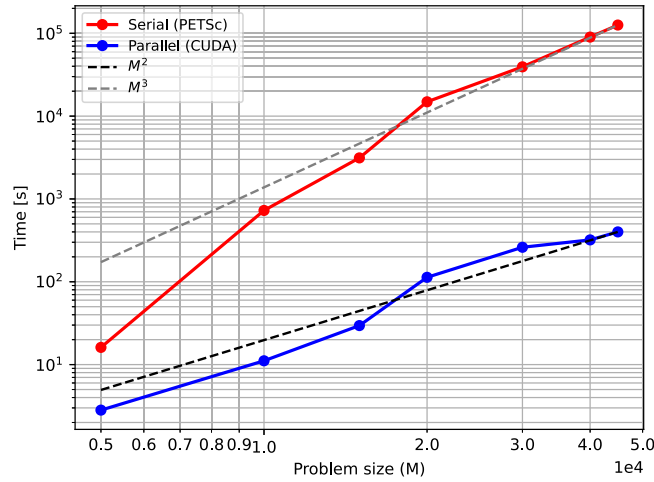
Fig. 17. Log-log comparison of computation times of the serial versus the parallel CUDA implementation of the LU solver for a single filament and for a cloud of 1000 filaments, discretized with an increasing number of degrees of freedom M. The parallel solver allows to improve performance from $\mathcal{O}(M^3)$ to $\mathcal{O}(M^2)$ and the CUDA solver is more than 300 times faster than the serial one (e.g. 314 times for $M = 45000$, which corresponds to 15000 nodes per filament).

Declaration of competing interest

The authors declare that they have no known competing financial interests or personal relationships that could have appeared to influence the work reported in this paper.

Data availability

Data will be made available on request.

Acknowledgements

Appendix A. Analytical calculation of the kernel integrals on straight segments

In this Appendix we describe the procedure that we have employed to evaluate the integrals in Equation (14) and compute the coefficients of the matrix in Equation (13). In this derivation, we closely follow and extend the work of Smith et al. [60], which showed that these integrals can be approximated by a sum of straight line integrals that can be evaluated analytically when the forces along each straight segment are uniform. Here, we show that analytical expressions can also be found when prescribing a linear variation of the forces on the beam straight segments.

We start the derivation from the line integral in the right hand side of Equation (10), which we report here for convenience:

$$\int_0^{\ell_e} \boldsymbol{S}(\boldsymbol{x}, \boldsymbol{y}(s)) \, \hat{\boldsymbol{f}}(s) \, |\boldsymbol{y}'(s)| \, ds. \tag{A.1}$$

The integral above can be simplified by a change of coordinates that will align the straight segment with the horizontal axis and translate to the origin one of the nodes of the segment, say $\boldsymbol{y}_0$, as in Fig. A.18. This transformation can be expressed as

$$\tilde{\boldsymbol{x}} = \boldsymbol{\Theta}_e^n \left(\boldsymbol{x} - \boldsymbol{y}_0 \right), \tag{A.2}$$

where $\boldsymbol{\Theta}_e^n$ is an appropriate rotation matrix. In this coordinate system the beam segment can be simply parametrized as $\boldsymbol{y}(s) = s\hat{\boldsymbol{e}}_1$ and the integral (A.1) can be rewritten as:
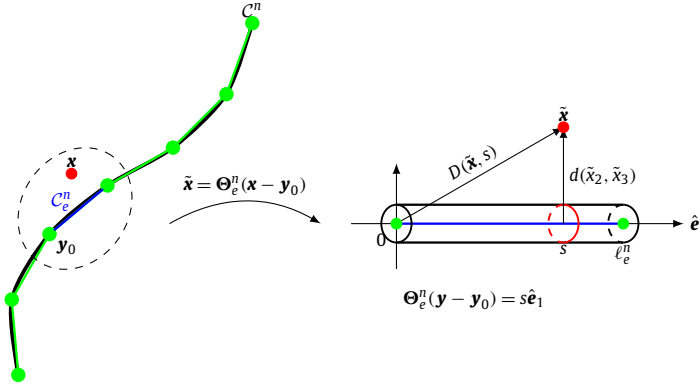
Fig. A.18. Schematic of the roto-translation of each element onto the reference element.

$$\int_0^{\ell_e} \mathbf{S}(\mathbf{x}, \mathbf{y}(s))\, \hat{\mathbf{f}}(s)\, |\mathbf{y}'(s)|\, ds = \int_0^{\ell_e} \left(\mathbf{\Theta}_e^n\right)^T \hat{\mathbf{S}}(\tilde{\mathbf{x}}, s) \mathbf{\Theta}_e^n \hat{\mathbf{f}}(s)\, |\mathbf{\Theta}_e^n \hat{\mathbf{e}}_1|\, ds, \tag{A.3}$$

where we have set $\hat{\mathbf{S}}(\tilde{\mathbf{x}}, s) = \mathbf{S}((\mathbf{\Theta}_e^n)^T \tilde{\mathbf{x}} + \mathbf{y}_0, s\hat{\mathbf{e}}_1)$. Note that $|\mathbf{\Theta}_e^n \hat{\mathbf{e}}_1| = 1$ because $\mathbf{\Theta}_e^n$ is a rotation matrix and $|\hat{\mathbf{e}}_1| = 1$.

Plugging the linear $\hat{\mathbf{f}}(s)$ discretization of Equation (11) into Equation (A.3), we obtain

$$\int_0^{\ell_e} \mathbf{S}(\mathbf{x}, \mathbf{y}(s))\, \hat{\mathbf{f}}(s)\, |\mathbf{y}'(s)| ds = \left(\mathbf{\Theta}_e^n\right)^T \sum_b \left(\int_0^{\ell_e} \hat{\mathbf{S}}(\tilde{\mathbf{x}}, s) N_f^b(s) ds \right) \hat{\mathbf{f}}^b \mathbf{\Theta}_e^n. \tag{A.4}$$

The integrals

$$\int_0^{\ell_e} \hat{\mathbf{S}}(\tilde{\mathbf{x}}, s) N_f^b(s)\, ds$$

can be obtained for any linear $N_f^b(s)$ as an appropriate linear combination of

$$\int_0^{\ell_e} \hat{\mathbf{S}}(\tilde{\mathbf{x}}, s)\, ds \tag{A.5}$$

and

$$\int_0^{\ell_e} \hat{\mathbf{S}}(\tilde{\mathbf{x}}, s) s\, ds. \tag{A.6}$$

After substituting the expression of the Stokeslet from Equation (6) we obtain

$$\hat{\mathbf{S}}(\tilde{\mathbf{x}}, s) =$$

$$\frac{1}{8\pi\mu}\frac{1}{D(\tilde{\mathbf{x}}, s)^3} \begin{bmatrix} 2(\tilde{x}_1 - s)^2 + \tilde{x}_2^2 + \tilde{x}_3^2 & (\tilde{x}_1 - s)\tilde{x}_2 & (\tilde{x}_1 - s)\tilde{x}_3 \\ (\tilde{x}_1 - s)\tilde{x}_2 & (\tilde{x}_1 - s)^2 + 2\tilde{x}_2^2 + \tilde{x}_3^2 & \tilde{x}_2\tilde{x}_3 \\ (\tilde{x}_1 - s)\tilde{x}_3 & \tilde{x}_2\tilde{x}_3 & (\tilde{x}_1 - s)^2 + \tilde{x}_2^2 + 2\tilde{x}_3^2 \end{bmatrix},$$

where we have set $D(\tilde{\mathbf{x}}, s) = \sqrt{(\tilde{x}_1 - s)^2 + \tilde{x}_2^2 + \tilde{x}_3^2}$. We have computed the integrals (A.5) and (A.6) analytically with the software Mathematica [83], obtaining the following analytical expressions:

$$\int_0^{\ell_e} \hat{\mathbf{S}}(\tilde{\mathbf{x}}, s)\, ds = \begin{bmatrix} I_{11} & I_{12} & I_{13} \\ I_{12} & I_{22} & I_{23} \\ I_{13} & I_{23} & I_{33} \end{bmatrix}, \quad \int_0^{\ell_e} \hat{\mathbf{S}}(\tilde{\mathbf{x}}, s) s\, ds = \begin{bmatrix} I_{11}^s & I_{12}^s & I_{13}^s \\ I_{12}^s & I_{22}^s & I_{23}^s \\ I_{13}^s & I_{23}^s & I_{33}^s \end{bmatrix},$$

where the components of the matrices are listed below:

$$I_{11} = 2\log\left(\frac{s - \tilde{x}_1 + D(\tilde{\boldsymbol{x}}, s)}{\sqrt{\tilde{x}_2^2 + \tilde{x}_3^2}}\right) - \frac{s - \tilde{x}_1}{D(\tilde{\boldsymbol{x}}, s)}, \tag{A.7}$$

$$I_{22} = \log\left(\frac{s - \tilde{x}_1 + D(\tilde{\boldsymbol{x}}, s)}{\sqrt{\tilde{x}_2^2 + \tilde{x}_3^2}}\right) + \frac{s - \tilde{x}_1}{D(\tilde{\boldsymbol{x}}, s)}\frac{\tilde{x}_2^2}{\tilde{x}_2^2 + \tilde{x}_3^2}, \tag{A.8}$$

$$I_{33} = \log\left(\frac{s - \tilde{x}_1 + D(\tilde{\boldsymbol{x}}, s)}{\sqrt{\tilde{x}_2^2 + \tilde{x}_3^2}}\right) + \frac{s - \tilde{x}_1}{D(\tilde{\boldsymbol{x}}, s)}\frac{\tilde{x}_3^2}{\tilde{x}_2^2 + \tilde{x}_3^2}, \tag{A.9}$$

$$I_{12} = I_{21} = \frac{\tilde{x}_2}{D(\tilde{\boldsymbol{x}}, s)}, \tag{A.10}$$

$$I_{13} = I_{31} = \frac{\tilde{x}_3}{D(\tilde{\boldsymbol{x}}, s)}, \tag{A.11}$$

$$I_{23} = I_{32} = \frac{s - \tilde{x}_1}{\psi}\frac{\tilde{x}_2\tilde{x}_3}{\tilde{x}_2^2 + \tilde{x}_3^2}, \tag{A.12}$$

$$I_{11}^s = 2\tilde{x}_1\log\left(\frac{s - \tilde{x}_1 + D(\tilde{\boldsymbol{x}}, s)}{\sqrt{\tilde{x}_2^2 + \tilde{x}_3^2}}\right) + \frac{3(\tilde{x}_2^2 + \tilde{x}_3^2)}{D(\tilde{\boldsymbol{x}}, s)} + \frac{(2s - 3\tilde{x}_1)(s - \tilde{x}_1)}{D(\tilde{\boldsymbol{x}}, s)}, \tag{A.13}$$

$$I_{22}^s = \tilde{x}_1\log\left(\frac{s - \tilde{x}_1 + D(\tilde{\boldsymbol{x}}, s)}{\sqrt{\tilde{x}_2^2 + \tilde{x}_3^2}}\right) + \frac{\tilde{x}_2^2 + \tilde{x}_3^2}{D(\tilde{\boldsymbol{x}}, s)} + \frac{\tilde{x}_1(s - \tilde{x}_1)}{D(\tilde{\boldsymbol{x}}, s)}\frac{\tilde{x}_2^2}{\tilde{x}_2^2 + \tilde{x}_3^2} + \frac{(s - \tilde{x}_1)^2 - \tilde{x}_2^2}{D(\tilde{\boldsymbol{x}}, s)}, \tag{A.14}$$

$$I_{33}^s = \tilde{x}_1\log\left(\frac{s - \tilde{x}_1 + D(\tilde{\boldsymbol{x}}, s)}{\sqrt{\tilde{x}_2^2 + \tilde{x}_3^2}}\right) + \frac{\tilde{x}_2^2 + \tilde{x}_3^2}{D(\tilde{\boldsymbol{x}}, s)} + \frac{\tilde{x}_1(s - \tilde{x}_1)}{D(\tilde{\boldsymbol{x}}, s)}\frac{\tilde{x}_3^2}{\tilde{x}_2^2 + \tilde{x}_3^2} + \frac{(s - \tilde{x}_1)^2 - \tilde{x}_3^2}{D(\tilde{\boldsymbol{x}}, s)}, \tag{A.15}$$

$$I_{12}^s = I_{21}^s = \tilde{x}_2\left[\frac{s}{D(\tilde{\boldsymbol{x}}, s)} - \log\left(\frac{s - \tilde{x}_1 + D(\tilde{\boldsymbol{x}}, s)}{\sqrt{\tilde{x}_2^2 + \tilde{x}_3^2}}\right)\right], \tag{A.16}$$

$$I_{13}^s = I_{31}^s = \tilde{x}_3\left[\frac{s}{D(\tilde{\boldsymbol{x}}, s)} - \log\left(\frac{s - \tilde{x}_1 + D(\tilde{\boldsymbol{x}}, s)}{\sqrt{\tilde{x}_2^2 + \tilde{x}_3^2}}\right)\right], \tag{A.17}$$

$$I_{23}^s = I_{32}^s = \frac{\tilde{x}_2\tilde{x}_3}{D(\tilde{\boldsymbol{x}}, s)}\left(\frac{\tilde{x}_1(s - \tilde{x}_1)}{\sqrt{\tilde{x}_2^2 + \tilde{x}_3^2}} - 1\right). \tag{A.18}$$

Note that, because the node $\tilde{\boldsymbol{x}}$ belongs to the boundary of the filament, then $D(\tilde{\boldsymbol{x}}, s) \geq \sqrt{\tilde{x}_2^2 + \tilde{x}_3^2} \geq a, \forall\tilde{\boldsymbol{x}}, \forall s$. Therefore, all integrals above are well-defined for any finite filament radius a.

Appendix B. Supplementary material

Supplementary material related to this article can be found online at https://doi.org/10.1016/j.jcp.2022.111774.

References

[1] D.A. Head, A.J. Levine, F.C. MacKintosh, Deformation of cross-linked semiflexible polymer networks, Phys. Rev. Lett. 91 (10) (2003), https://doi.org/10.1103/PhysRevLett.91.108102.
[2] R.H. Pritchard, Y.Y. Shery Huang, E.M. Terentjev, Mechanics of biological networks: from the cell cytoskeleton to connective tissue, Soft Matter 10 (12) (2014) 1864–1884, https://doi.org/10.1039/c3sm52769g.
[3] M.L. Gardel, F. Nakamura, J.H. Hartwig, J.C. Crocker, T.P. Stossel, D.A. Weitz, Prestressed F-actin networks cross-linked by hinged filamins replicate mechanical properties of cells, Proc. Natl. Acad. Sci. USA 103 (6) (2006) 1762–1767, https://doi.org/10.1073/pnas.0504777103.
[4] T. Shinar, M. Mana, F. Piano, M.J. Shelley, A model of cytoplasmically driven microtubule-based motion in the single-celled Caenorhabditis elegans embryo, Proc. Natl. Acad. Sci. USA (2011), https://doi.org/10.1073/pnas.1017369108.

[5] E.W. Wong, P.E. Sheehan, C.M. Lieber, Nanobeam mechanics: elasticity, strength, and toughness of nanorods and nanotubes, Science 277 (5334) (1997) 1971–1975, https://doi.org/10.1126/science.277.5334.1971.

[6] M.R. Falvo, G.J. Clary, R.M. Taylor, V. Chi, F.P. Brooks, S. Washburn, R. Superfine, Bending and buckling of carbon nanotubes under large strain, Nature 389 (6651) (1997) 582–584, https://doi.org/10.1038/39282.

[7] K.I. Jang, H.U. Chung, S. Xu, C.H. Lee, H. Luan, J. Jeong, H. Cheng, G.T. Kim, S.Y. Han, J.W. Lee, J. Kim, M. Cho, F. Miao, Y. Yang, H.N. Jung, M. Flavin, H. Liu, G.W. Kong, K.J. Yu, S.I. Rhee, J. Chung, B. Kim, J.W. Kwak, M.H. Yun, J.Y. Kim, Y.M. Song, U. Paik, Y. Zhang, Y. Huang, J.A. Rogers, Soft network composite materials with deterministic and bio-inspired designs, Nat. Commun. 6 (2015), https://doi.org/10.1038/ncomms7566.

[8] B. Bharti, A.L. Fameau, M. Rubinstein, O.D. Velev, Nanocapillarity-mediated magnetic assembly of nanoparticles into ultraflexible filaments and recon-figurable networks, Nat. Mater. 14 (11) (2015) 1104–1109, https://doi.org/10.1038/nmat4364.

[9] R. Mhanna, F. Qiu, L. Zhang, Y. Ding, K. Sugihara, M. Zenobi-Wong, B.J. Nelson, Artificial bacterial flagella for remote-controlled targeted single-cell drug delivery, Small 10 (10) (2014) 1953–1957, https://doi.org/10.1002/smll.201303538.

[10] R. Dreyfus, J. Baudry, M.L. Roper, M. Fermigier, H.A. Stone, J. Bibette, Microscopic artificial swimmers, Nature (2005), https://doi.org/10.1038/nature04090.

[11] T. Su, P.K. Purohit, Semiflexible filament networks viewed as fluctuating beam-frames, Soft Matter 8 (17) (2012) 4664–4674, https://doi.org/10.1039/c2sm07058h.

[12] M.K. Jawed, N.K. Khouri, F. Da, E. Grinspun, P.M. Reis, Propulsion and instability of a flexible helical rod rotating in a viscous fluid, Phys. Rev. Lett. 115 (2015) 168101, https://doi.org/10.1103/PhysRevLett.115.168101.

[13] G.K. Batchelor, Sedimentation in a dilute dispersion of spheres, J. Fluid Mech. 52 (2) (1972) 245–268, https://doi.org/10.1017/S0022112072001399.

[14] K. Adachi, S. Kiriyama, N. Yoshioka, The behavior of a swarm of particles moving in a viscous fluid, Chem. Eng. Sci. 33 (1) (1978) 115–121, https://doi.org/10.1016/0009-2509(78)85077-5.

[15] J.M. Nitsche, G.K. Batchelor, Break-up of a falling drop containing dispersed particles, J. Fluid Mech. 340 (1997) 161–175, https://doi.org/10.1017/S0022112097005223.

[16] R.H. Davis, A. Acrivos, Sedimentation of noncolloidal particles at low Reynolds numbers, Annu. Rev. Fluid Mech. 17 (1985) 91–118, https://doi.org/10.1146/annurev.fl.17.010185.000515.

[17] D.L. Koch, E.S. Shaqfeh, The instability of a dispersion of sedimenting spheroids, J. Fluid Mech. 209 (1989) 521–542, https://doi.org/10.1017/S0022112089003204.

[18] B. Herzhaft, É. Guazzelli, M.B. Mackaplow, E.S. Shaqfeh, Taylor experimental investigation of the sedimentation of a dilute fiber suspension, Phys. Rev. Lett. 77 (2) (1996) 290–293, https://doi.org/10.1103/PhysRevLett.77.290.

[19] M.B. Mackaplow, E.S. Shaqfeh, A numerical study of the sedimentation of fibre suspensions, J. Fluid Mech. 376 (1998) 149–182, https://doi.org/10.1017/S0022112098002663.

[20] B. Herzhaft, É. Guazzelli, Experimental study of the sedimentation of dilute and semi-dilute suspensions of fibres, J. Fluid Mech. 384 (1999) 133–158, https://doi.org/10.1017/S0022112099004152.

[21] J.E. Butler, E.S. Shaqfeh, Dynamic simulations of the inhomogeneous sedimentation of rigid fibres, J. Fluid Mech. 468 (2002) 205–237, https://doi.org/10.1017/S0022112002001544.

[22] D. Saintillan, E. Darve, E.S. Shaqfeh, A smooth particle-mesh Ewald algorithm for Strokes suspension simulations: the sedimentation of fibres, Phys. Fluids 17 (3) (2005), https://doi.org/10.1063/1.1862262.

[23] B. Metzger, É. Guazzelli, J.E. Butler, Large-scale streamers in the sedimentation of a dilute fiber suspension, Phys. Rev. Lett. 95 (16) (2005) 2, https://doi.org/10.1103/PhysRevLett.95.164506.

[24] B. Metzger, M. Nicolas, É. Guazzelli, Falling clouds of particles in viscous fluids, J. Fluid Mech. 580 (2007) 283–301, https://doi.org/10.1017/S0022112007005381.

[25] J. Park, B. Metzger, É. Guazzelli, J.E. Butler, A cloud of rigid fibres sedimenting in a viscous fluid, J. Fluid Mech. 648 (2010) 351–362, https://doi.org/10.1017/S0022112009993909.

[26] S. Alben, M. Shelley, J. Zhang, Drag reduction through self-similar bending of a flexible body, Nature 420 (2002) 479–481, https://doi.org/10.1038/nature01232.

[27] F. Gosselin, E. De Langre, B.A. Machado-Almeida, Drag reduction of flexible plates by reconfiguration, J. Fluid Mech. 650 (2010) 319–341, https://doi.org/10.1017/S0022112009993673.

[28] M. Manghi, X. Schlagberger, Y. Kim, R. Netz, Hydrodynamic effects in driven soft matter, Soft Matter 2 (2006) 653–668, https://doi.org/10.1039/b516777a.

[29] T. Witten, H. Diamant, A review of shaped colloidal particles in fluids: anisotropy and chirality, Rep. Prog. Phys. 83 (2020) 116601, https://doi.org/10.1088/1361-6633/abb5c4.

[30] M. Bukowicki, M.L. Ekiel-Jeżewska, Different bending models predict different dynamics of sedimenting elastic trumbbells, Soft Matter 14 (2018) 5786–5799.

[31] O. du Roure, A. Lindner, E.N. Nazockdast, M.J. Shelley, Dynamics of flexible fibers in viscous flows and fluids, Annu. Rev. Fluid Mech. (2019), https://doi.org/10.1146/annurev-fluid-122316-045153.

[32] A.K. Tornberg, K. Gustavsson, A numerical method for simulations of rigid fiber suspensions, J. Comput. Phys. 215 (1) (2006) 172–196, https://doi.org/10.1016/j.jcp.2005.10.028.

[33] K. Gustavsson, A.K. Tornberg, Gravity induced sedimentation of slender fibers, Phys. Fluids 21 (12) (2009) 1–15, https://doi.org/10.1063/1.3273091.

[34] T. Bosse, L. Kleiser, C. Härtel, E. Meiburg, Numerical simulation of finite Reynolds number suspension drops settling under gravity, Phys. Fluids 17 (3) (2005) 037101, https://doi.org/10.1063/1.1851428.

[35] G. Machu, W. Meile, L.C. Nitsche, U. Schaflinger, Coalescence, torus formation and breakup of sedimenting drops: experiments and computer simula-tions, J. Fluid Mech. 447 (2001) 299–336, https://doi.org/10.1017/S0022112001005882.

[36] G.C. Abade, F.R. Cunha, Computer simulation of particle aggregates during sedimentation, Comput. Methods Appl. Mech. Eng. 196 (45) (2007) 4597–4612, https://doi.org/10.1016/j.cma.2007.05.022.

[37] F. Bülow, H. Nirschl, W. Dörfler, On the settling behaviour of polydisperse particle clouds in viscous fluids, Eur. J. Mech. B, Fluids 50 (2015) 19–26, https://doi.org/10.1016/j.euromechflu.2014.11.003.

[38] O. Ayeni, S.S. Tiwari, C. Wu, J.B. Joshi, K. Nandakumar, Behavior of particle swarms at low and moderate Reynolds numbers using computational fluid dynamics—discrete element model, Phys. Fluids 32 (7) (2020) 073304, https://doi.org/10.1063/5.0008518.

[39] Y. Lin, J.H. Tan, N. Phan-Thien, B.C. Khoo, Settling of particle-suspension drops at low to moderate Reynolds numbers, Eur. J. Mech. B, Fluids 61 (2017) 72–76, https://doi.org/10.1016/j.euromechflu.2016.11.003.

[40] E. Nazockdast, A. Rahimian, D. Zorin, M. Shelley, A fast platform for simulating semi-flexible fiber suspensions applied to cell mechanics, J. Comput. Phys. 329 (2017) 173–209, https://doi.org/10.1016/j.jcp.2016.10.026.

[41] S.F. Schoeller, A.K. Townsend, T.A. Westwood, E.E. Keaveny, Methods for suspensions of passive and active filaments, J. Comput. Phys. 424 (2021), https://doi.org/10.1016/j.jcp.2020.109846.

[42] X. Xu, A. Nadim, Deformation and orientation of an elastic slender body sedimenting in a viscous liquid, Phys. Fluids 6 (9) (1994) 2889–2893, https://doi.org/10.1063/1.868116.

[43] M.C. Lagomarsino, I. Pagonabarraga, C.P. Lowe, Hydrodynamic induced deformation and orientation of a microscopic elastic filament, Phys. Rev. Lett. (2005), https://doi.org/10.1103/PhysRevLett.94.148104.

[44] L. Li, H. Manikantan, D. Saintillan, S.E. Spagnolie, The sedimentation of flexible filaments, J. Fluid Mech. (2013), https://doi.org/10.1017/jfm.2013.512.

[45] G. Saggiorato, J. Elgeti, R.G. Winkler, G. Gompper, Conformations, hydrodynamic interactions, and instabilities of sedimenting semiflexible filaments, Soft Matter (2015), https://doi.org/10.1039/c5sm01069a.

[46] A.-K. Tornberg, M.J. Shelley, Simulating the dynamics and interactions of flexible fibers in Stokes flows, J. Comput. Phys. 196 (1) (2004) 8–40, https://doi.org/10.1016/j.jcp.2003.10.017.

[47] H. Manikantan, D. Saintillan, Effect of flexibility on the growth of concentration fluctuations in a suspension of sedimenting fibers: particle simulations, Phys. Fluids 28 (1) (2016), https://doi.org/10.1063/1.4938493.

[48] O. Maxian, A. Mogilner, A. Donev, Integral-based spectral method for inextensible slender fibers in Stokes flow, Phys. Rev. Fluids 6 (2021) 14102–14157, https://doi.org/10.1103/PhysRevFluids.6.014102.

[49] X. Schlagberger, R.R. Netz, Orientation of elastic rods in homogeneous Stokes flow, Europhys. Lett. 70 (2005) 129–135, https://doi.org/10.1209/epl/i2004-10461-5.

[50] I. Llopis, I. Pagonabarraga, M.C. Lagomarsino, C.P. Lowe, Sedimentation of pairs of hydrodynamically interacting semiflexible filaments, Phys. Rev. E, Stat. Nonlinear Soft Matter Phys. 76 (2007) 061901, https://doi.org/10.1103/PhysRevE.76.061901.

[51] B. Delmotte, E. Climent, F. Plouraboué, A general formulation of Bead Models applied to flexible fibers and active filaments at low Reynolds number, J. Comput. Phys. 286 (2015) 14–37, https://doi.org/10.1016/j.jcp.2015.01.026.

[52] B. Marchetti, V. Raspa, A. Lindner, O. Du Roure, L. Bergougnoux, É. Guazzelli, C. Duprat, Deformation of a flexible fiber settling in a quiescent viscous fluid, Phys. Rev. Fluids (2018), https://doi.org/10.1103/PhysRevFluids.3.104102.

[53] A.M. Słowicka, E. Wajnryb, M.L. Ekiel-Jeewska, Dynamics of flexible fibers in shear flow, J. Chem. Phys. 143 (12) (2015) 124904, https://doi.org/10.1063/1.4931598.

[54] T. Sasayama, M. Inagaki, Simplified bead-chain model for direct fiber simulation in viscous flow, J. Non-Newton. Fluid Mech. 250 (2017) 52–58, https://doi.org/10.1016/j.jnnfm.2017.11.001.

[55] T. Sasayama, M. Inagaki, Efficient bead-chain model for predicting fiber motion during molding of fiber-reinforced thermoplastics, J. Non-Newton. Fluid Mech. 264 (2019) 135–143, https://doi.org/10.1016/j.jnnfm.2018.10.008.

[56] C.J. Cyron, W.A. Wall, Finite-element approach to Brownian dynamics of polymers, Phys. Rev. E, Stat. Nonlinear Soft Matter Phys. 80 (6) (2009), https://doi.org/10.1103/PhysRevE.80.066704.

[57] L. Greengard, V. Rokhlin, A fast algorithm for particle simulations, J. Comput. Phys. 135 (2) (1997) 280–292, https://doi.org/10.1016/0021-9991(87)90140-9.

[58] C. Meier, A. Popp, W.A. Wall, A locking-free finite element formulation and reduced models for geometrically exact Kirchhoff rods, Comput. Methods Appl. Mech. Eng. 290 (2015) 314–341, https://doi.org/10.1016/j.cma.2015.02.029.

[59] C. Meier, A. Popp, W.A. Wall, A finite element approach for the line-to-line contact interaction of thin beams with arbitrary orientation, Comput. Methods Appl. Mech. Eng. 308 (2016) 377–413, https://doi.org/10.1016/j.cma.2016.05.012.

[60] D.J. Smith, A boundary element regularized Stokeslet method applied to cilia- and flagella-driven flow, Proc. R. Soc. A, Math. Phys. Eng. Sci. (2009), https://doi.org/10.1098/rspa.2009.0295.

[61] P. Wriggers, G. Zavarise, On contact between three-dimensional beams undergoing large deflections, Commun. Numer. Methods Eng. 13 (6) (1997) 429–438, https://doi.org/10.1002/(SICI)1099-0887(199706)13:6<429::AID-CNM70>3.0.CO;2-X.

[62] G.K. Batchelor, Slender-body theory for particles of arbitrary cross-section in Stokes flow, J. Fluid Mech. (1970), https://doi.org/10.1017/S002211207000191X.

[63] C. Meier, W.A. Wall, A. Popp, A unified approach for beam-to-beam contact, Comput. Methods Appl. Mech. Eng. 315 (2017) 972–1010, https://doi.org/10.1016/j.cma.2016.11.028.

[64] J.M. Stockie, S.I. Green, Simulating the motion of flexible pulp fibres using the immersed boundary method, J. Comput. Phys. 147 (1) (1998) 147–165, https://doi.org/10.1006/jcph.1998.6086.

[65] S. Lim, C.S. Peskin, Simulations of the whirling instability by the immersed boundary method, SIAM J. Sci. Comput. 25 (6) (2004) 2066–2083, https://doi.org/10.1137/S1064827502417477.

[66] J.K. Wiens, J.M. Stockie, Simulating flexible fiber suspensions using a scalable immersed boundary algorithm, Comput. Methods Appl. Mech. Eng. 290 (2015) 1–18, https://doi.org/10.1016/j.cma.2015.02.026.

[67] L. Zhu, C.S. Peskin, Simulation of a flapping flexible filament in a flowing soap film by the immersed boundary method, J. Comput. Phys. 179 (2) (2002) 452–468, https://doi.org/10.1006/jcph.2002.7066.

[68] L. Zhu, R.C.Y. Chin, Simulation of elastic filaments interacting with a viscous pulsatile flow, Comput. Methods Appl. Mech. Eng. 197 (25) (2008) 2265–2274, https://doi.org/10.1016/j.cma.2007.11.031.

[69] R.-N. Hua, L. Zhu, X.-Y. Lu, Dynamics of fluid flow over a circular flexible plate, J. Fluid Mech. 759 (2014), https://doi.org/10.1017/jfm.2014.571.

[70] Y. Kim, C.S. Peskin, Penalty immersed boundary method for an elastic boundary with mass, Phys. Fluids 19 (2007), https://doi.org/10.1063/1.2734674.

[71] Y. Kim, C.S. Peskin, A penalty immersed boundary method for a rigid body in fluid, Phys. Fluids 28 (2016) 033603, https://doi.org/10.1063/1.4944565.

[72] C. Pozrikidis, Boundary Integral and Singularity Methods for Linearized Viscous Flow, Cambridge University Press, 1992.

[73] R.G. Cox, The motion of long slender bodies in a viscous fluid. Part 1. General theory, J. Fluid Mech. 44 (04) (1970) 791, https://doi.org/10.1017/S002211207000215X.

[74] J. Lighthill, Flagellar hydrodynamics, SIAM Rev. 18 (2) (1976) 161–226, https://doi.org/10.1137/1018040.

[75] R.E. Johnson, An improved slender-body theory, J. Fluid Mech. 99 (2) (1980) 411–431, https://doi.org/10.1017/S0022112080000687.

[76] R. Cortez, The method of regularized stokeslets, SIAM J. Sci. Comput. 23 (4) (2002) 1204–1225, https://doi.org/10.1137/S106482750038146X.

[77] R. Cortez, L. Fauci, A. Medovikov, The method of regularized Stokeslets in three dimensions: analysis, validation, and application to helical swimming, Phys. Fluids (2005), https://doi.org/10.1063/1.1830486.

[78] R. Cortez, Regularized Stokeslet segments, J. Comput. Phys. 375 (1) (2018) 783–796, https://doi.org/10.1016/j.jcp.2018.08.055.

[79] D.J. Smith, A nearest-neighbour discretisation of the regularized stokeslet boundary integral equation, J. Comput. Phys. 358 (2018) 88–102, https://doi.org/10.1016/j.jcp.2017.12.008.

[80] The **ΣMIT** Development Group, ΣMIT, a scalable computational framework for large-scale simulation of complex mechanical response of materials, http://summit.mit.edu, 2021.

[81] S. Balay, J. Brown, P. Brune, K. Buschelman, L. Dalcin, V. Eijkhout, W. Gropp, D. Karpeyev, D. Kaushik, M. Knepley, L.C. McInnes, B. Smith, S. Zampini, H. Zhang, Petsc users manual, Tech. Rep. ANL-95/11 - Revision 3.13, Argonne National Laboratory, 2020, https://petsc.org.

[82] NVIDIA, P. Vingelmann, F.H. Fitzek, Cuda, release: 10.2.89, https://developer.nvidia.com/cuda-toolkit, 2020.

[83] W.R. Inc, Mathematica, version 12.0.0, Champaign, IL, https://www.wolfram.com/mathematica, 2020.